

From seismic models to mantle temperatures: Uncertainties related to mineralogical complexities and limited tomographic resolution

Gabriel Robl¹, Bernhard S.A. Schuberth¹, Isabel Papanagnou¹
and Christine Thomas²

¹Ludwig–Maximilians–Universität München, Dept. of Earth and Environmental Sciences, Munich 80333, Germany. E-mail: gabriel.rob@lmu.de

²Universität Münster, Dept. of Physics, Münster 48149, Germany

Accepted 2025 April 16. Received 2025 March 7; in original form 2024 October 15

SUMMARY

Many geophysical studies require knowledge on the present-day temperature distribution in Earth's mantle. One example is geodynamic inverse models, which utilize data assimilation techniques to reconstruct mantle flow back in time. The thermal state of the mantle can be estimated from seismic velocity perturbations imaged by tomography with the help of thermodynamic models of mantle mineralogy. Unique interpretations of the tomographically imaged seismic heterogeneity can either be obtained by incorporating additional data sets or requires assumptions on the chemical composition of the mantle. However, even in the case of (assumed) known chemical composition, both the seismic and the mineralogical information are significantly affected by inherent limitations and different sources of uncertainty. Here, we investigate the theoretical ability to estimate the thermal state of the mantle from tomographic models in a synthetic closed-loop experiment. The 'true' temperature distribution of the mantle is taken from a 3-D mantle circulation model with Earth-like convective vigour. We aim to recover this reference model after: (1) mineralogical mapping from the 'true' temperatures to seismic velocities, (2) application of a tomographic filter to mimic the effect of limited seismic resolution, and (3) mapping of the 'imaged' seismic velocities back to temperatures. We test and quantify the interplay of tomographically damped and blurred seismic heterogeneity in combination with different approximations for the mineralogical 'inverse' conversion from seismic velocities to temperature. Owing to imperfect knowledge of the parameters governing mineral anelasticity, we additionally investigate the effects of over- or underestimating the corresponding correction to the underlying mineralogical model. Our results highlight that, given the current limitations of seismic tomography and the incomplete knowledge of mantle mineralogy, magnitudes and spatial scales of a temperature field obtained from global seismic models deviate significantly from the true state, even in the idealized case of known bulk chemical composition. The average deviations from the reference model are on the order of 50–100 K in the upper mantle and depending on the resolving capabilities of the respective tomography—can increase with depth throughout the lower mantle to values of up to 200 K close to the core–mantle boundary. Furthermore, large systematic errors exist in the vicinity of phase transitions due to the associated mineralogical complexities. When used to constrain buoyancy forces in time-dependent geodynamic simulations, errors in the temperature field might grow nonlinearly due to the chaotic nature of mantle flow. This could be particularly problematic in combination with advanced implementations of compressibility, in which densities are extracted from thermodynamic mineralogical models with temperature-dependent phase assemblages. Erroneous temperatures in this case might activate 'wrong' phase transitions and potentially flip the sign of the associated Clapeyron slopes, thereby considerably altering the model evolution. Additional testing is required to evaluate the behaviour of different compressibility formulations in geodynamic inverse problems. Overall, the strategy to estimate the present-day thermodynamic state of the mantle must be selected carefully to minimize the influence of the collective set of uncertainties.

Key words: Composition and structure of the mantle; Phase transitions; Seismic tomography.

1 INTRODUCTION

Mantle convection is driven by thermally dominated buoyancy forces in Earth's interior. Direct observations of the 3-D temperature variations in the mantle are not available, but inferences can in principle be drawn from seismic observations. These provide the most abundant and direct source of information on Earth's deep interior. Tomographic models, in particular, inferred from the seismic data through inversion, provide insight into the present-day structure of the mantle. Thanks to the enormous progress in data acquisition, numerical methods and computational resources over the last 40 yr, global seismic models are getting closer to resolving mantle features at the dynamically relevant length scales (e.g. Rawlinson *et al.* 2010; French & Romanowicz 2014; Simmons *et al.* 2021; Fichtner *et al.* 2024). Many promising research directions have been identified that will further improve and diversify tomographic efforts in the near future (Fichtner *et al.* 2024). One aspect that is only recently shifting into the focus of seismic tomography relates to the quantification of resolution and uncertainties (Rawlinson *et al.* 2014; Fichtner & van Leeuwen 2015; Zaroli 2016; Freissler *et al.* 2024; Cui *et al.* 2024). This is particularly relevant, because even though many tomographic models correlate well at large scales, small scale structures of less than 1000 km are generally not uniquely resolved, and tomographic images can still differ fundamentally at these scales (Becker & Boschi 2002; Dziewonski 2005; Liu & Gu 2012; Lebedev *et al.* 2017; Cui *et al.* 2024). To derive robust estimates of the present-day temperature distribution in the mantle from tomography, we thus need to understand the uncertainties caused by the complex relationship between seismic and thermodynamic mantle properties, and in particular their combination with limited tomographic resolution.

Alternative to the seismic data approach, physically driven expectations on mantle structure can be gained from geodynamic forward simulations. However, many of the governing material properties to date still need to be constrained more robustly, most notably the mantle viscosity. To further progress in this direction, geodynamic inverse modelling based on the concept of mathematical adjoints has been established as a promising tool (e.g. Bunge *et al.* 2003; Ismail-Zadeh *et al.* 2004; Horbach *et al.* 2014; Colli *et al.* 2018; Ghelichkhan *et al.* 2021). These inverse models are designed to solve for an unknown initial condition that naturally evolves into the present-day state as seen by tomography. By iterative refinement of the initial state, the models minimize the differences between the tomographically imaged mantle and the predictions of a forward mantle circulation model (MCM). Although mantle flow is chaotic and subject to the butterfly effect, it has been shown that robust flow histories can nevertheless be constructed through assimilation of horizontal flow velocities as surface boundary condition (Colli *et al.* 2015; Taiwo *et al.* 2023). The great benefit of inverse geodynamic models is that they produce model trajectories from the geologic past to the present, which, if simulated at sufficiently high Rayleigh number, should provide accurate estimates of the true mantle evolution. Using independent data sets sensitive to the surface expression of mantle convection, such as dynamic topography/the geoid (e.g. Richards & Hager 1984; Hoggard *et al.* 2021; Lin *et al.* 2022) or geologic records of vertical motion (Hayek *et al.* 2020; Vilacis *et al.* 2022), then allows testing the model evolution against

observations and placing tighter constraints on the validity of the underlying parameters.

One vital element of geodynamic inverse models is an accurate representation of the present-day thermal mantle structure derived from seismic observations. The same is true for instantaneous flow calculations that aim at modelling the geoid (e.g. Hager *et al.* 1985) or compare tomographically derived mantle flow velocities to measurements of seismic anisotropy (Becker *et al.* 2008; Long & Becker 2010). Under the commonly adopted assumption that variations in seismic velocity are predominantly controlled by temperature together with potential variations in chemical composition, a multitude of studies have relied on interpreting seismic information in terms of the thermal or thermochemical state of the crust and mantle; using qualitative links and simple linear scaling laws, or sophisticated modelling and probabilistic approaches, to relate the observed seismic velocities to temperature and associated densities (e.g. Forte *et al.* 1995; Sobolev *et al.* 1996; Deal *et al.* 1999; Goes *et al.* 2000; Forte & Mitrova 2001; Deschamps *et al.* 2002, 2019; Deschamps & Trampert 2003; Priestley & McKenzie 2006; Khan *et al.* 2008, 2011; Ritsema *et al.* 2009; Cammarano *et al.* 2011; Priestley & McKenzie 2013; Afonso *et al.* 2013, 2016; Munch *et al.* 2020; Deschamps & Cobden 2022; Ramirez *et al.* 2022). New concepts that aim to optimize seismic imaging techniques for a direct inversion for temperature are presently emerging (Fullea *et al.* 2021; Lebedev *et al.* 2024), which allow to bypass non-unique seismic inversion solutions and ensure physically plausible temperature distributions. The seismic properties of the mantle are herein assumed to be largely composition-insensitive (Lebedev *et al.* 2024).

Nowadays, thermodynamic models of mantle mineralogy serve as the basis to self-consistently model the nonlinear relationship between temperature and seismic velocity in the mantle, while incorporating relevant effects of phase transformations together with their dependence on temperature and pressure (e.g. Connolly 2005; Piazzoni *et al.* 2007; Stixrude & Lithgow-Bertelloni 2011, 2021, 2024; Holland *et al.* 2013; Chust *et al.* 2017). Within these mineralogical models, stable phase assemblages are computed for a given bulk composition by Gibbs-free-energy minimization of the candidate phases and their solid solutions. In combination with large experimental databases on mantle minerals, easy-to-use lookup-tables can be created, providing the link between thermodynamic condition (pressure, temperature, composition) and the elastic properties of interest (seismic velocities, thermal expansivity, etc.), as well as density. From the mineralogical models, the relationship between temperature and (elastic) seismic velocity is found to be complex and nonlinear, seemingly invalidating the usability of a simple linearized temperature-velocity scaling. The largest non-linearities are generally attributed to pressure-induced solid–solid mineral phase transitions (e.g. Stixrude & Lithgow-Bertelloni 2007), such as those in the mantle transition zone (TZ). The associated sharp jumps of mineral properties are observable as global seismic discontinuities (e.g. Shearer 2000; Deuss 2009), and are a recurring feature in 1-D seismic reference profiles (e.g. Dziewoński & Anderson 1981; Kennett *et al.* 1995). Since phase transformation depths in the mantle are sensitive to temperature, lateral thermal variations cause regional undulations of the seismically visible interfaces. The topography of various discontinuities has thus been the focus of many studies (e.g. Flanagan & Shearer 1998; Gu & Dziewoński 2002; Lawrence

& Shearer 2006; Schmerr & Garnero 2006; Ritsema *et al.* 2009), providing independent constraints on mantle temperatures at the respective depths.

In the mantle, the two most prominent discontinuities are linked to the transformation of olivine to wadsleyite, occurring at roughly 410 km depth, and the dissociation of ringwoodite to bridgmanite and ferropericlase, at roughly 660 km depth (Ringwood 1968). We follow common abbreviations and refer to the two discontinuities as the ‘410’ and the ‘660’ from here on. With the transformation from bridgmanite, the most abundant mineral in the lower mantle, to the post-perovskite phase (pPv), another important phase transition has been discovered in the lowermost mantle (Murakami *et al.* 2004; Hirose 2006). While the lateral extent of pPv occurrence is debated (Cobden *et al.* 2015; Thomas *et al.* 2022), the presence of this high-pressure phase could be a potential explanation for many intriguing seismic observation close to the core–mantle boundary (e.g. Shim 2008; Davies *et al.* 2015; Lay 2015; Koelemeijer *et al.* 2018).

In the TZ, important dynamic implications arise from the fact that the 410 and 660 phase transitions have opposite Clapeyron slopes, and therefore opposite effects on vertical mass transport (Christensen & Yuen 1984; Bina & Helffrich 1994; Christensen 1995). While the exothermic transition associated with the 410 supports mantle flow, the 660 transition is endothermic, potentially interfering with flow across the TZ. Early tomographic images already indicated substantial mass exchange between upper and lower mantle, although often featuring complex slab morphologies near the 660 (Fukao *et al.* 1992; Grand 1994; Grand *et al.* 1997; van der Hilst *et al.* 1997; Masters *et al.* 2000), which has subsequently been interpreted as an indication of (temporarily) impeded mantle flow across the endothermic interface (e.g. Christensen 2001; Fukao *et al.* 2009). The influence of the 660 on global-scale mantle convection has been extensively studied (e.g. Christensen & Yuen 1984, 1985; Bercovici *et al.* 1993; Tackley *et al.* 1993; Christensen 1995; Schubert & Tackley 1995; Bunge *et al.* 1997; Nolet *et al.* 2006; Thomas & Billen 2009; van Mierlo *et al.* 2013; Papanagnou *et al.* 2022), yet open questions remain regarding its imprint on the characteristics of convection.

Alongside the mineralogical complexities, inferences on the present-day thermodynamic state of the mantle from tomographic models are additionally hindered by the fact that the seismic resolution is naturally limited by uneven data coverage—due to an uneven distribution of both earthquakes and receivers around the globe—and the need for regularization in seismic inversions. As a consequence, global tomographic models represent a blurred and low-fidelity image of the true mantle structure. For meaningful comparisons between geodynamic and tomographic models, the resolution discrepancies need to be taken into account by tomographic filtering of the geodynamic model (e.g. Mégnin *et al.* 1997; Bunge & Davies 2001; Ritsema *et al.* 2007; Schuberth *et al.* 2009b), which mimics how a given (hypothetical) input structure would be imaged by a specific tomographic inversion. This process is computationally simple, but requires resolution information for the respective tomographic model to be explicitly available in the form of a resolution matrix or generalized inverse (Freissler *et al.* 2020). The necessity of tomographic filtering to link geodynamic and tomographic models has been increasingly acknowledged and incorporated in the past decade (e.g. Bull *et al.* 2009; Davies *et al.* 2012; Koelemeijer *et al.* 2018; Simmons *et al.* 2019; Su *et al.* 2023; Freissler *et al.* 2024).

Deriving temperatures from seismic observations is thus subject to various assumptions and uncertainties, even in the simplified case

of homogeneous chemical composition. Using the aforementioned mineralogical models, the seismic velocities obtained by tomography can generally be translated to temperature in a straightforward manner. However, little attention has been paid so far to the combined effects of tomographic and mineralogical limitations. The uncertainties of thermodynamic parameters in mineralogical models, as well as their propagation to temperature inferences, have been estimated earlier (e.g. Cammarano *et al.* 2003; Khan *et al.* 2008; Connolly & Khan 2016), but to our knowledge, no such study has explicitly included the effects of reduced-amplitude and blurred seismic velocities due to limited tomographic resolution. Bull *et al.* (2010) on the other hand investigated the influence of tomographic resolution together with different approaches to derive density perturbations from seismic velocities on calculated flow fields of geodynamic models. However, they employed simplified velocity-density scalings that do not account for realistic complexity induced by phase transitions. To this end, we systematically and quantitatively assess the coupled effects of limited resolution and complex mineralogical relationships on the recoverability of accurate present-day thermal models in a synthetic closed-loop setup. Additionally, we assess further contributions from uncertainties in the necessary anelastic correction and assumed bulk composition. We aim to quantify first-order effects of various uncertainties in the simplest case of an isochemical model, since possible chemical variations introduce large additional complexities (see Munch *et al.* 2020; Cobden *et al.* 2024). We begin by introducing the concept and individual methods of the closed-loop experiment, followed by outlining the effects of different uncertainties individually, as well as their potential interplay. We investigate different approaches and common approximations used for the conversion of seismic velocities to temperature and discuss their advantages and disadvantages as well as the potential dynamic implications of the associated errors for geodynamic simulations.

2 METHODS—CLOSED-LOOP SETUP

In order to assess the theoretical ability to estimate the present-day thermal mantle structure from seismic models, we employ a synthetic closed-loop experiment. The starting point of the loop is the 3-D temperature field from a pre-existing isochemical MCM (Nerlich *et al.* 2016). With a dense radial and lateral grid spacing on the order of 25 km globally, mantle flow was simulated at Earth-like convective vigour in this MCM. Temperature variations in such models are controlled by the dynamics of the system, and thus show realistic length scales and magnitudes (Schuberth *et al.* 2009a, b). Owing to the fact that tectonic plate reconstructions are incorporated as time-varying surface velocity boundary condition, the model characteristics furthermore are largely independent of the (unknown) initial condition (Colli *et al.* 2015). With the thermal structure being reasonably Earth-like in a statistical sense as well as in terms of the broader geographical distribution, we take the final (i.e. geologic present-day) state of the geodynamic model as a representation of the true temperature distribution in the mantle. Further technical details on the input model are provided in Appendix A.

The concept of the closed-loop is summarized in Fig. 1. The ‘true’ 3-D temperature field is taken from the reference MCM, either from the model directly or from a reparametrized version. The reparametrization step at the start of the loop is necessary to apply a tomographic filter in order to mimic the limited resolution of seismic tomography. Both concepts are further outlined in

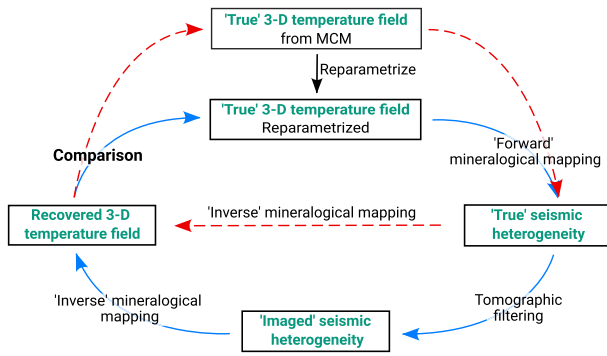


Figure 1. Closed-loop setup, starting from the 3-D temperature field of a mantle circulation model. In case a tomographic filter is applied in the loop, an additional reparametrization step of the input temperature field is required (see Section 2.1). The reparametrized temperatures then act as the ‘true’ reference model, thereby allowing us to omit the mathematically necessary (but non-physical) step of reparametrization from the final comparison (solid, blue loop). Under the idealized assumption of perfect tomographic resolution (i.e. without tomographic filtering), no reparametrization is required, and the reference model is the temperature field of the MCM directly (dashed, red loop).

the following subsection. Using a thermodynamic model of mantle mineralogy (Chust *et al.* 2017), we initially convert the ‘true’ model temperatures into seismic velocities. This way, non-linearities in the relation between thermal and seismic structure are incorporated, in particular the relevant effects of phase transitions as well as their dependence on pressure and temperature. We call this the ‘forward’ mineralogical mapping, through which we derive the ‘true’ seismic heterogeneity from the thermal heterogeneity of the starting model. As a second step, we apply a tomographic filter to the ‘true’ seismic heterogeneity, to account for the limited resolution of seismic tomography. The ‘imaged’ seismic heterogeneity after tomographic filtering thus represents a synthetic tomographic model that is compatible with the ‘true’ reference temperature field. Taking the same mineralogical model used to realize the ‘forward’ mineralogical mapping (i.e. to convert from temperature to seismic velocity), a consistent ‘inverse’ mineralogical mapping can be performed, converting the tomographically filtered seismic velocities back to temperature. Alternatively, approximations of the mineralogical model can be employed to convert from seismic velocity to temperature, which simplify the nonlinear (and non-bijective) mineralogical relationships (for details see Section 2.2). At the end of the closed-loop, we recover a 3-D temperature field, which can be directly compared to the ‘true’ reference, allowing us to quantitatively evaluate the differences. Without considering additional sources of uncertainty, the misfit between reference and recovered model showcases the full amount of information that is lost due to tomographic limitations and the difficulties related to the complexity of the mineralogical mapping. The three major tools used in this study are:

- (i) a high-resolution 3-D mantle convection model, from which we take the present-day temperature distribution as the ‘true’ mantle structure with realistic amplitudes and length scales,
- (ii) thermodynamic models of mantle mineralogy, to convert between temperatures and seismic velocities,
- (iii) and tomographic filtering, to account for limited seismic resolution.

All three tools are described in further detail in the subsequent sections and the Appendix.

2.1 Tomographic filtering

Tomographic filtering allows for meaningful comparisons between seismic tomography and geodynamic models; that is, the hypothetical ‘true’ mantle, by mimicking how a given input structure would be imaged in a respective tomographic inversion. Here, this step is performed by multiplying the ‘true’ model with the resolution operator \mathcal{R} , as described in Ritsema *et al.* (2007). \mathcal{R} is specific to a tomographic model and fully characterizes its spatially heterogeneous resolution and the effects of damping. Explicit calculation of \mathcal{R} is computationally demanding, especially for larger tomographic problems. Therefore, only a few full resolution operators have been published so far (e.g. Boschi 2003; Soldati & Boschi 2005; Ritsema *et al.* 2007, 2011; Koelemeijer *et al.* 2016; Bogiatzis *et al.* 2016; Simmons *et al.* 2019). To assess the variable characteristics of different tomographic filters and their specific resolving power on our results, we test all global tomographic models for which we have \mathcal{R} explicitly available. These encompass the S -wave models S20RTS (Ritsema *et al.* 1999, 2004) and S40RTS (Ritsema *et al.* 2011), and the joint P - and S -wave models SP12RTS (Koelemeijer *et al.* 2016) and LLNL-G3D-JPS (Simmons *et al.* 2015, from hereon abbreviated as LLNL). The S++RTS-family of models is parametrized in spherical harmonics laterally and splines vertically and represents a broad spectrum of resolution: the long-wavelength model SP12RTS that incorporates normal-mode data, the earlier S20RTS model considered intermediate resolution here, and the comparatively high-resolution model S40RTS. The LLNL model in contrast is parametrized in local basis functions on an (almost) equidistant grid and locates at the upper end of the resolution spectrum considered here. Our analysis thus covers a representative range of the properties of available tomographic models.

One general characteristic of tomographic models is their inability to resolve the sharp velocity variations induced by phase transitions (Romanowicz 2003). After tomographic filtering, this (non-)feature is reproduced in our synthetic setup (Fig. 2). Consequently, loss of amplitudes due to limited resolution is generally largest in depths of seismic discontinuities, strongly limiting the interpretability of these depth regions in terms of temperature.

A complication in the closed-loop experiment arises from the fact that tomographic filtering can only be performed on geodynamic models represented in the same parametrization as the respective tomography. Modern geodynamic models are usually calculated on dense numerical grids, with typical grid spacing in the range of 10–50 km. The spatial parametrization of current global traveltimes tomographies on the other hand differs by at least one order of magnitude (e.g. Zanolli 2016; Simmons *et al.* 2021), with typical grid resolution on the order of hundreds of kilometres. The ‘true’ structure of the geodynamic input model therefore needs to be projected onto the tomographic grid before filtering; that is, a reparametrization is required, which constitutes an unphysical, but unavoidable step in the general work flow. There are two options when to perform this procedure in our closed-loop setup: Specifically, one can choose whether the ‘true’ temperatures or rather the ‘true’ seismic velocities are projected to the tomographic grid; in other words, whether the reparametrization is implemented before or after the nonlinear forward mineralogical mapping. Depending on the magnitude of grid spacing differences between geodynamic and tomographic model, reparametrization alone can have a strong, depth-dependent effect on the ‘resolved’ length scales and amplitudes of model heterogeneities (Schuberth *et al.* 2009b). When the reparametrization is performed with respect to the conversion to seismic velocities therefore determines whether or not sharp seismic discontinuities

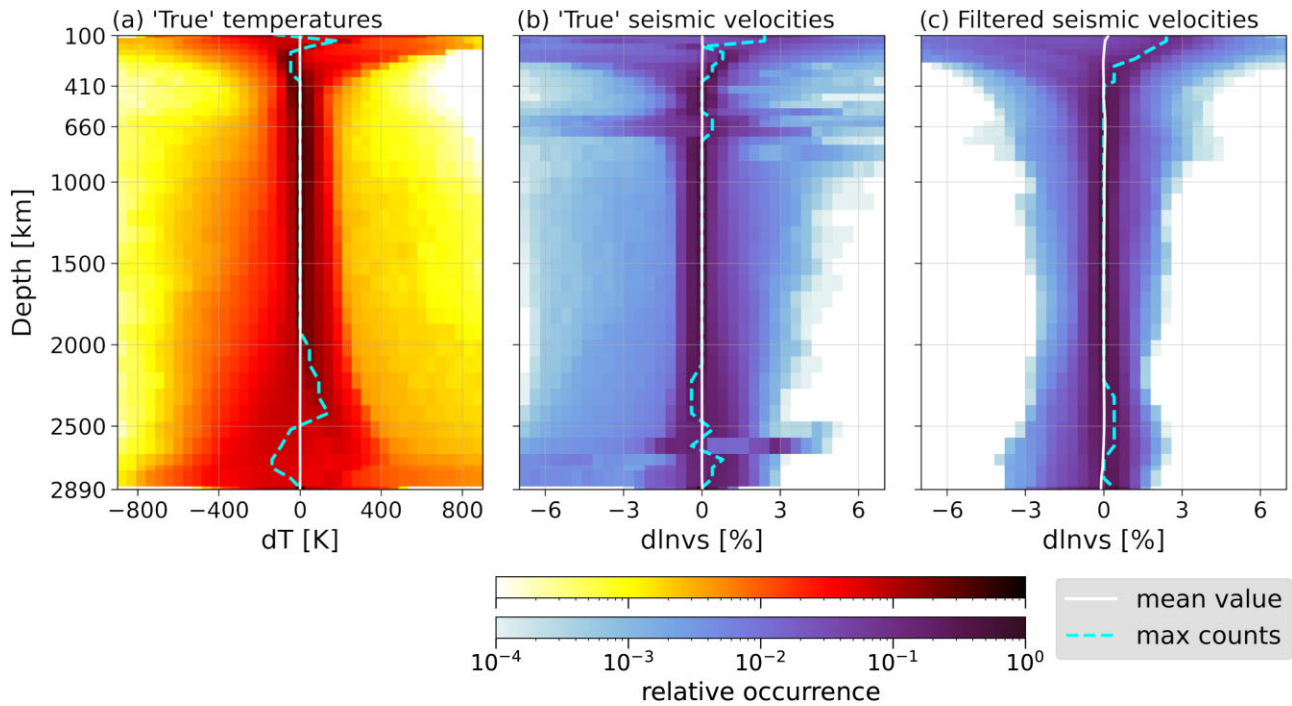


Figure 2. Depth-dependent histograms of the distribution of temperature/seismic velocity variations. Counts in each depth are normalized to the total number of grid points per layer (163 842), so that the values in each horizontal row sum to 1. The histograms show (a) the ‘true’ temperature field given by the reference MCM, (b) the corresponding ‘true’ seismic heterogeneity and (c) the ‘imaged’ seismic heterogeneity after tomographic filtering with the resolution operator of S40RTS. Note that strong seismic perturbations in the ‘true’ seismic velocities are generated in regions of phase transitions from an initially smooth temperature field, particularly at 660 and at ~ 2600 km depth. After tomographic filtering, the strong perturbations are almost completely smoothed out due to the limited resolving power of the seismic inversion. Temperatures are mapped to seismic velocities using the original mineralogical table (see Section 2.2). After tomographic filtering in the spherical harmonics domain (i.e. with either of the S++RTS filters), the seismic velocities are expanded back onto the grid of the unfiltered reference MCM, therefore keeping the same amount of grid points per layer.

are smoothed out in the ‘true’ seismic structure. However, as tomographic filtering leads to further smoothing and damping, differences between the two possibilities in the resulting ‘imaged’ seismic heterogeneity are negligible for all tomographic filters used in this study (Figs D1 and D2). Instead, choosing between the two options mainly determines whether the recovered temperature field can be evaluated against the initial MCM or its reparametrized version (i.e. which model to use as reference). This is because a reparametrized temperature field consistent with the parametrization of the chosen tomographic model is only available when the forward mineralogical mapping is performed afterwards. In previous studies involving tomographic filtering, reparametrization is commonly performed in the seismic domain (e.g. Schuberth *et al.* 2009b; Bull *et al.* 2009; Davies *et al.* 2012; Koelemeijer *et al.* 2018; Simmons *et al.* 2019). In this study, we chose to reparametrize in temperature and use the reparametrized model as reference (Fig. 1, blue loop). This way, we isolate the physical errors due to tomographic filtering from the unphysical, but mathematically necessary reparametrization effects. The results of this study therefore represent a minimum estimate of the limitations due to the physical resolution effects only, when inferring global temperature distributions from seismic models. Under the (idealized) assumption of perfect tomographic resolution, one can also choose to omit seismic filtering in the loop by converting the ‘true’, unfiltered seismic heterogeneity directly back to temperature using one of the mineralogical inverse mappings. The temperature field of the initial MCM acts as reference then, because reparametrization is not required in this case (Fig. 1, red loop).

2.2 Mineralogical forward and inverse mapping

To compute the mineralogical tables, which list the elastic parameters and density for a discrete set of pressure and temperature values, we use the software *MMA-EoS* (Chust *et al.* 2017). The code incorporates the widely adopted thermodynamic database of Stixrude & Lithgow-Bertelloni (2011). Alternative databases exist (e.g. Connolly 2005; Piazzoni *et al.* 2007; Stixrude & Lithgow-Bertelloni 2024), but we do not expect them to significantly change the systematic findings of this study. We derive stable mineral assemblages for a six-oxide NCFMAS system (Na_2O , CaO , FeO , MgO , Al_2O_3 , SiO_2), which accounts for ~ 99 mol per cent of a pyrolite chemical composition (Chust *et al.* 2017). The detailed oxide proportions are listed in table C1. Pyrolite in turn has been found to be a reasonable choice for bulk mantle composition, reconciling for example the magnitude of observed seismic velocities and their lateral gradients in the lower mantle (Schuberth *et al.* 2009a; Davies *et al.* 2012; Zhang *et al.* 2013), global traveltimes statistics (Schuberth *et al.* 2012) and the occurrence of phase transformations in the TZ and lowermost mantle at the expected conditions (Murakami *et al.* 2005; Koelemeijer *et al.* 2018; Ishii *et al.* 2018). Additional complexities from potential chemical heterogeneity are deliberately avoided by keeping the composition fixed throughout the mantle. Assuming a purely thermal origin of mantle heterogeneity is consistent with the isochemical input MCM and allows for a unique interpretation of the seismic structure in terms of temperature. In a later section, we nevertheless briefly explore the effects of a mismatch between the bulk compositions applied in the forward and inverse mineralogical conversion,

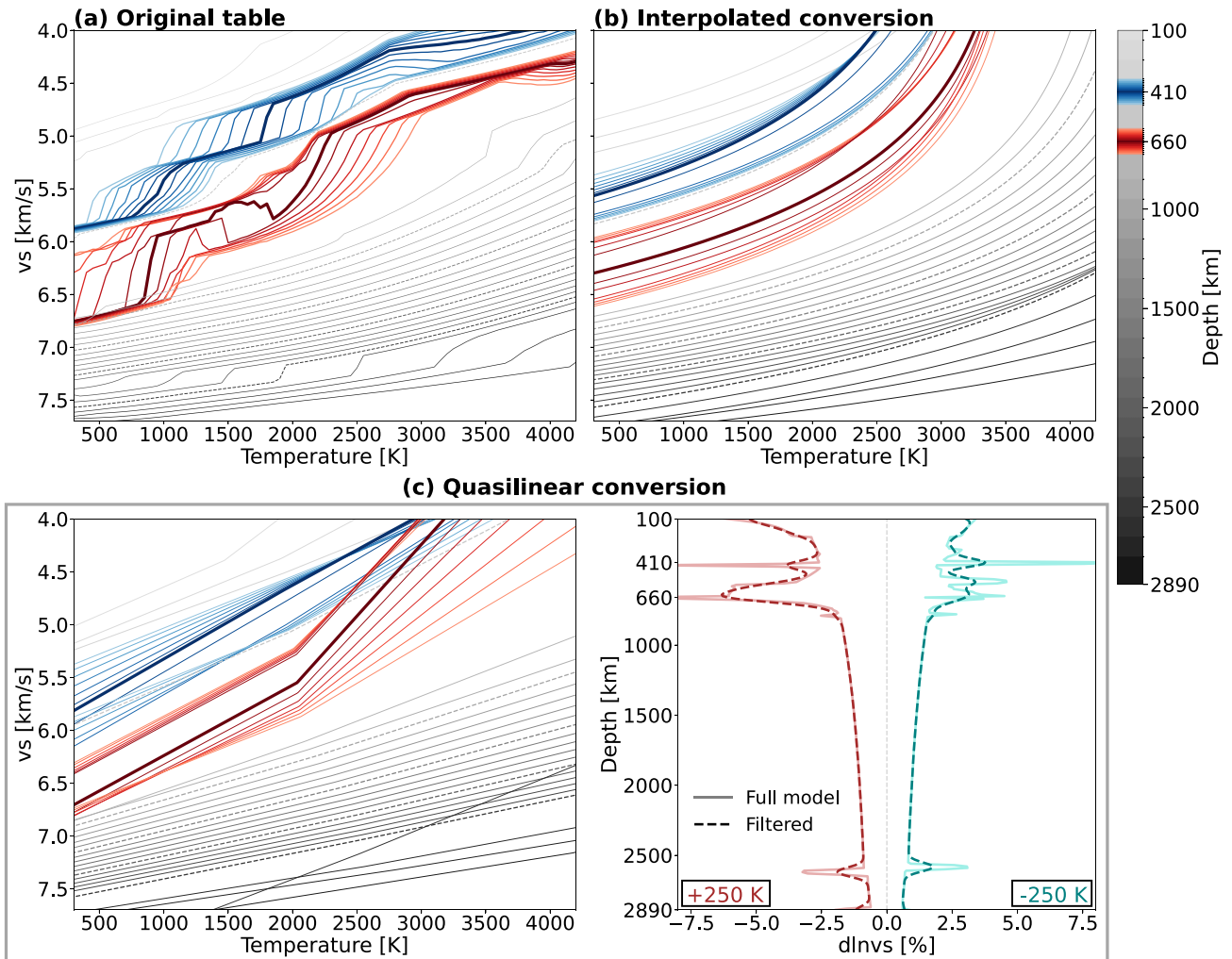


Figure 3. Relation between shear-wave velocity and temperature given by the three versions of the mineralogical model that are used to convert seismic velocities to temperature. (a) The original mineralogical table, (b) its smoothed, interpolated form (Colli *et al.* 2018) and (c) the quasilinear conversion method. Each line in (a, b, c/left) represents the T - v_s -relation at one discrete depth, indicated by the colour. Dashed lines represent multiples of 500 km in depth. The data is illustrated this way, because for the inverse mapping with the original mineralogical data, the algorithm searches along one of those lines—determined by the specified depth and starting from the mean temperature—for a suitable temperature matching the given seismic velocity. (c/right) Depth-dependent temperature derivatives of seismic velocity used for the quasilinear conversion, evaluated at ± 250 K around the mean temperature (separately for positive and negative values). The derivatives (solid lines) are smoothed with a Gaussian filter (dashed lines) before extracting the scaling factors.

such as a mechanical mixture of depleted mantle and bulk oceanic crust.

The thermodynamic lookup-tables contain the temperature- and pressure-dependent elastic properties of the bulk rock in increments of 50 K and 0.1 GPa, respectively. We restrict this study to the results obtained from a conversion to shear-wave velocities (v_s), as v_s -models commonly provide better global data coverage than models of compressional-wave velocities (v_p). Together with the greater temperature-dependence of v_s compared to v_p , this makes shear-wave velocities more widely applicable for the thermal interpretation of seismic models. Additionally, of the four tomographic filters available to us, two underlying tomographic models exclusively provide information on v_s (S20RTS and S40RTS). Fig. 3(a) illustrates the relation between temperature and shear-wave velocity, determined from the lookup-tables. The mineralogical model integrates the simple, almost linear temperature-dependence of v_s in the mid- to lower mantle on one hand, and the highly nonlinear

relation between the parameters in the presence of phase transitions on the other hand (410 and 660 km highlighted in thick blue and red, respectively). Steeper slopes in the figure represent increased temperature sensitivity of the seismic velocities. They are largest in the vicinity of phase transitions, indicative of sudden changes in material properties that produce the prominent sharp jumps in radial seismic profiles. On average, these synthetically predicted transformations agree well with the observed depths of seismic discontinuities (Cammarano *et al.* 2009; Deuss 2009; Papanagnou *et al.* 2022).

In order to relate the thermal structure of the geodynamic input model to its according seismic structure in a forward sense, we always use the mineralogical model in its original form, as acquired from *MMA-EoS*. This way, we ensure that the temperature variations obtained from the geodynamic model, which inherently are rather smooth, translate into the expected ‘rough’ seismic structure across phase transitions (see Fig. 2b). For the inverse conversion from

seismic velocities to temperatures on the other hand, we explore three approaches that are all derived from the thermodynamic mineralogical model—its original form and two approximate versions:

(i) Conversion with the original table

The most natural choice for mapping seismic velocities to temperature is to utilize the same, unaltered lookup-tables that are employed for the forward conversion (Fig. 3a). This way, the full non-linear complexity of the assumed ‘true’ mineralogical behaviour is captured. Since the occurrence of phase transitions is a self-consistent consequence of this *original* approach, it would—in case of perfect seismic resolution—convert a realistic seismic structure with discontinuities back into a smooth temperature field. Deviations from the ‘true’ seismic velocities, as is the case in any real tomography, will however propagate into the recovered temperatures and introduce dynamically unexpected disturbances. A considerable drawback of the original approach is the non-bijectionality of the temperature–seismic-velocity mapping around the negative Clapeyron-slope transition at the 660 (negative-slope section in Fig. 3a between ca. 1500 and 1800 K), where one seismic velocity can potentially be explained by multiple temperatures. Note that further regions of similar non-uniqueness exist in the parameter space of the mineralogical model, but not for plausible mantle conditions.

(ii) Interpolated conversion

To avoid the non-uniqueness problems of the original approach and to ensure that the obtained temperature field does not contain physically unexpected and numerically challenging jumps, Colli *et al.* (2018) used an approximated version of the original lookup-table for their inverse geodynamic models. This *interpolated* conversion is based on an exponential fit, tied to a seismic reference profile ($v_{s,1D}$),

$$\exp(v_s) = \alpha T + \exp(v_{s,1D}) \quad (1)$$

with α determined as the best-fit parameter for each depth. Fig. 3(b) shows the resulting interpolated temperature–velocity relation, visualized in the same way as the original data, for comparison. While the fit to the original data is good away from phase transitions, larger complexities, particularly in the TZ, are almost completely lost in the approximated model.

(iii) Quasilinear conversion

As a third method, we adopt the classical and widely used linearization of the mineralogical information. Prior to the establishment of sophisticated thermodynamic mineralogical models, studies in which seismic observations were interpreted in terms of mantle temperature or density usually relied on such simplified linear scaling laws (e.g. Hager *et al.* 1985; Stacey 1998; Forte & Mitrovia 2001; Cammarano *et al.* 2003; Deschamps & Trampert 2003; Goes *et al.* 2004). Variants of this approximation range from using just a globally constant scaling factor for the entire mantle to a depth-dependent or depth- and sign-dependent linear scaling between the parameters. In order to be best compatible with the original mineralogical inverse mapping, we follow the latter approach by determining temperature derivatives of seismic velocities from the original mineralogical model at ± 250 K around the mean temperature of the geodynamic input model, separately for each depth and sign of the seismic anomaly. (Fig. 3c, right panel). The choice of ± 250 K for the determination of the derivatives is somewhat arbitrary. We tested values between 50 and 500 K, with no fundamental differences on the results, so we chose to adopt the value of 250 K from Goes *et al.* (2004).

The resulting derivatives are then used to linearize the conversion between shear-wave velocity and temperature for positive and negative anomalies independently. Because of this split between positive and negative, providing two independent linear scaling factors per depth, we call this the *quasilinear* approach. Evaluating the complex mineralogical model in temperature ranges that cross phase transitions produces large derivatives, reaching values close to 10 per cent for temperature changes of 250 K. While this is expected for thermal perturbations that induce a phase change, it leads to small seismic anomalies being translated to erroneously small temperature variations. To avoid this, and to be representative of earlier studies, we applied a Gaussian filter to the derivatives (dashed lines in Fig. 3c, right panel) and used the filtered curves for the determination of the scaling values instead. Both the filtered and unfiltered curves highlight the expected decreasing sensitivity to temperature changes with depth (Trampert *et al.* 2001; Cammarano *et al.* 2003), with strongly increased values in the vicinity of phase transitions (Stixrude & Lithgow-Bertelloni 2007). Clear sensitivity peaks exist at 410 and 660 km as well as for the pPv-transition around 2600 km depth, with obvious asymmetry between positive and negative anomalies in the TZ. Additionally, one can also observe the self-consistent appearance of discontinuity topography from the mineralogical model, where peak sensitivities are located at different depths between warmer and colder anomalies (clearly visible for the 410 and pPv, less so for the more complex 660).

The resulting scaling relation between temperature and v_s is shown in the left panel of Fig. 3(c), again in the same fashion as the two previous approaches. Similar to the interpolated table, the fit outside of phase transitions is good, whereas the complex behaviour in the TZ and for pPv is poorly reproduced.

2.3 Anelastic correction

Minerals behave anelastically, especially at the high pressure–temperature conditions of the deep mantle, but the anelastic effects on the temperature–seismic-velocity scaling are poorly constrained. The material parameters in the databases entering the mineralogical models are based on high-frequency experimental data, where anelastic effects are negligible. In the much lower frequency range of teleseismic waves, however, intrinsic attenuation reduces wave propagation velocities and amplitudes due to dissipative processes, especially at high temperatures. This effect needs to be taken into account in the interpretation of seismic models, but its relative importance with respect to the anharmonic (i.e. purely elastic) contribution is still strongly debated. For instance, over thirty years ago, Karato (1993) already stated that anelasticity must be considered when relating results of seismic tomography to the thermal state of the mantle. Trampert *et al.* (2001) on the other hand found that its effects are likely negligible in the lower mantle, while newer studies argue that anelasticity must in fact be taken into account throughout the whole mantle (e.g. Matas & Bukowinski 2007; Schubert & Bigalke 2021). On the contrary, according to Karato & Karki (2001), the anelastic contribution to the temperature sensitivities of seismic velocities could be as high as their elastic counterpart.

To allow meaningful thermal interpretations of seismic models, the mineralogical tables thus need to be corrected for the effects of anelasticity. Nowadays, the elastic thermodynamic parameters of the relevant mantle minerals are constrained to within a few per cent (e.g. Stixrude & Lithgow-Bertelloni 2024), translating to an (elastic) v_s uncertainty of ~ 5 per cent (Connolly & Khan 2016). The poorly understood contribution of anelasticity further contributes to

the uncertainty of the effective, anelastic mantle properties (Cammarano *et al.* 2009). In this study, we follow the anelastic correction approach of Karato (1993), also adopted by e.g. Kuskov *et al.* (2006), Matas & Bukowinski (2007), Stixrude & Lithgow-Bertelloni (2007), Goes *et al.* (2012) and Schuberth & Bigalke (2021). Seismic velocities are adjusted for anelasticity based on the seismic quality factor Q_s , determined from a radial Q -profile together with local temperature deviations from a 1-D reference. This approach is beneficial in our synthetic setup, compared to the estimation of Q_s based on homologous temperature (e.g. Cammarano *et al.* 2003, 2011; Goes *et al.* 2004; Ghelichkhan *et al.* 2021), because we have full knowledge of the radial average temperature in the geodynamic models (which, however, is not well constrained for Earth). Uncertainties in the anelastic correction itself primarily stem from poorly understood parameters governing the anelastic contribution to seismic wavespeeds. These include the activation energy and the factor of frequency dependence of attenuation, and their complex dependencies on pressure, temperature, phase, grain size, etc. Similarly, the radial behaviour of Q_s is also insufficiently constrained, and many different profiles exist in the literature (see e.g. Romanowicz & Durek 2000; Schuberth & Bigalke 2021). Fluids like water or partial melts are not considered in our solid-state mineralogical models. Their presence in the mantle would however further increase seismic attenuation (e.g. Cobden *et al.* 2018). Additional details on the anelastic correction are provided in Appendix B.

For the purpose of this study, we test the influence of the uncertain anelastic contribution by exploiting the fact that we can independently switch on or off the correction for the forward and inverse mineralogical mapping within the closed-loop. Additionally to the standard case, where we assume perfect knowledge of anelasticity by applying the same (and thus consistent) correction to forward and inverse conversion, we explore two scenarios:

- (i) The anelastic correction is applied in the forward conversion from temperatures to seismic velocities (which represents the ‘true Earth’ in our closed-loop). The inverse mapping is, however, performed with the uncorrected, elastic values, thereby mimicking a general underestimation of the anelastic effects.
- (ii) The anelastic correction is not used in the forward conversion, but later applied in the inverse mapping, which mimics an overestimation of the effects of anelasticity.

3 RESULTS

In this section, we evaluate and quantify the fit between reference and recovered temperature field at the final stage of the closed-loop. First, we investigate the errors introduced through the three different mineralogical approaches used to convert from seismic velocities back to temperature by assuming perfect tomographic resolution and no additional uncertainties. Following this, we step-by-step add limitations and uncertainties to the evaluation. Most importantly, we assess the effects of limited tomographic resolution and its complex interaction with the approximate mineralogies. Afterwards, we add the effects of uncertainties in anelasticity and bulk composition by independently varying the relevant parameters in the forward and inverse mapping.

3.1 Effects of mineralogical inverse mapping

We isolate the effects introduced through the mineralogical inverse mapping by considering perfect tomographic resolution. This is

easily achieved by skipping the tomographic filtering step in the closed-loop. The ‘true’ seismic velocities are directly converted back to temperatures with each of the three conversion approaches, while all other parameters are kept constant. This scenario thus assumes no influence of additional uncertainties from tomography, anelasticity, composition, etc.

Fig. 4 shows the temperature distribution of the reference model at four different depths, together with the errors after recovering temperatures with each of the three conversion options. Note that in this ‘perfect resolution’ scenario, the reference model that acts as the ‘true’ structure is the unparametrized MCM (i.e. unaltered on the numerical grid of the underlying geodynamic simulation). This corresponds to the red closed-loop variant in Fig. 1. Errors are determined as simple point-by-point differences between reference and recovered temperature fields. The depths are chosen to cover the three most relevant phase transitions (410, 660 and pPv-transition between 2600 and 2700 km). Additionally, we show a mid-mantle section at roughly 1500 km, where the T - v_s relation in the mineralogical model is simple and well reproduced by both approximate mineralogies. For a complete evaluation with depth, we plot histograms of the mismatch between reference and recovered models (Fig. 5).

When using the original mineralogy in the unfiltered case, the reference temperature field can be recovered almost perfectly at all depths (Fig. 5a), with the only exception around the 660-discontinuity, where the endothermic phase change causes a non-bijective temperature–velocity relation. This represents a non-unique interaction between temperature and discontinuity topography, which cannot be resolved by sole knowledge of the seismic velocities. Utilizing the interpolated or quasilinear approach, large recovery errors can clearly be linked to phase transition effects in the forward mineralogy. The associated large velocity variations of the ‘true’ seismic heterogeneity (Fig. 2b) can, in contrast to the original mineralogy, no longer be explained by either of the two simplified inverse mappings. The recovered models therefore need vastly increased temperature anomalies in the respective depths to account for the velocity jumps. Resulting error amplitudes are on the order of ± 300 K, comparable in magnitude to the TZ thermal heterogeneity of the underlying MCM itself. Both approximations perform similarly well in depths away from phase transformations, with errors of less than 100 K for the majority of grid points. The nature of the misfit is complex, even outside of phase changes, and varies with the mineralogical conversion method, despite the apparent similarities of the two approximations at first glance. For instance, for extreme temperature variations, the linear approximation deviates to a larger extent from the nonlinear T - v_s relation of the original mineralogical model, but with opposing effect: using the quasilinear conversion, hotter-than-average temperatures are systematically overestimated, while lower-than-average temperatures are systematically underestimated, resulting in predominantly negative differences in the corresponding histogram (Fig. 5c). The interpolated conversion gives a better fit to the temperature extremes, resulting in a more symmetric histogram, at the cost of larger errors for moderate temperature perturbations (Fig. 5b).

3.2 Effects of limited tomographic resolution

For the realistic scenario of non-perfect seismic resolution, we now include the step of tomographic filtering in the closed-loop. Instead of the ‘true’ seismic velocities, we subsequently convert the

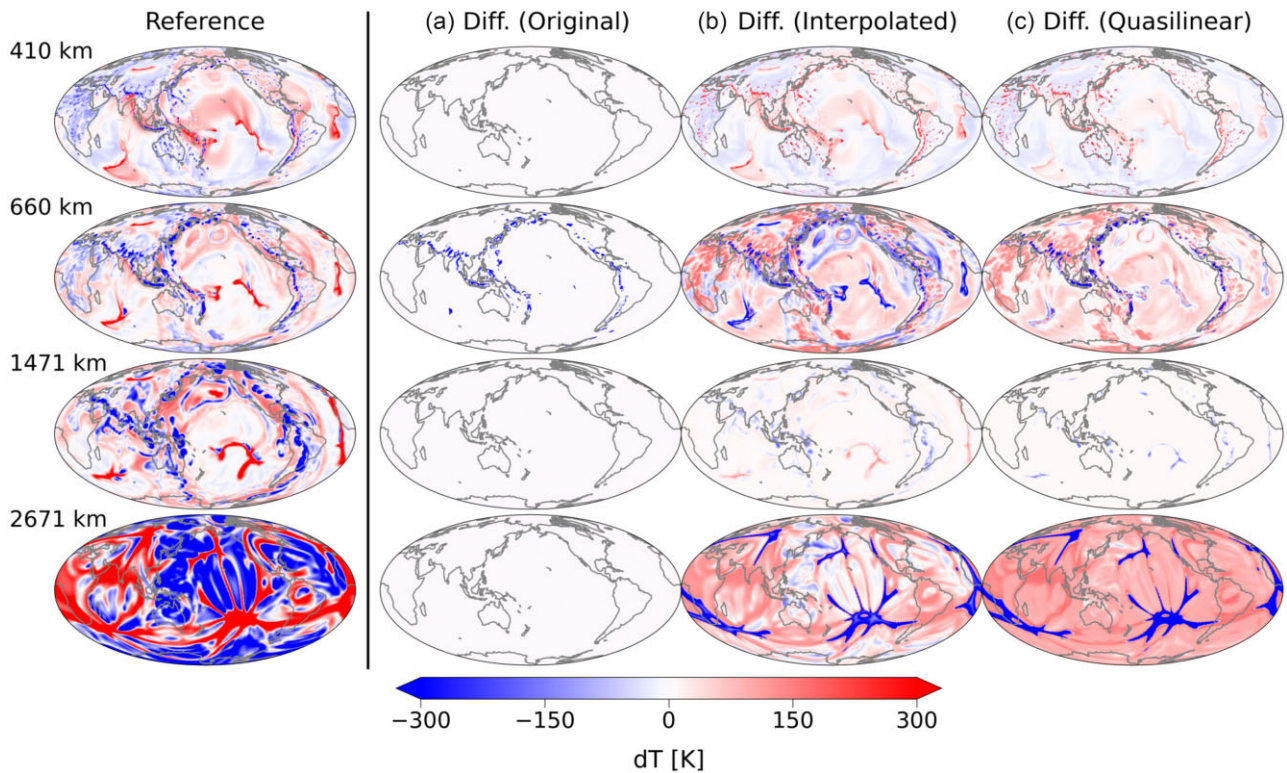


Figure 4. (Left column) Temperature anomalies of the reference mantle circulation model at four different depths, and (columns a–c) the respective point-by-point differences between the reference and the recovered temperature fields using (a) the original, (b) the interpolated and (c) the quasilinear version of the mineralogical model. Temperatures were recovered from the ‘true’ seismic heterogeneity (i.e. omitting the tomographic filtering step in the closed-loop), thus representing the idealized case of perfect seismic resolution.

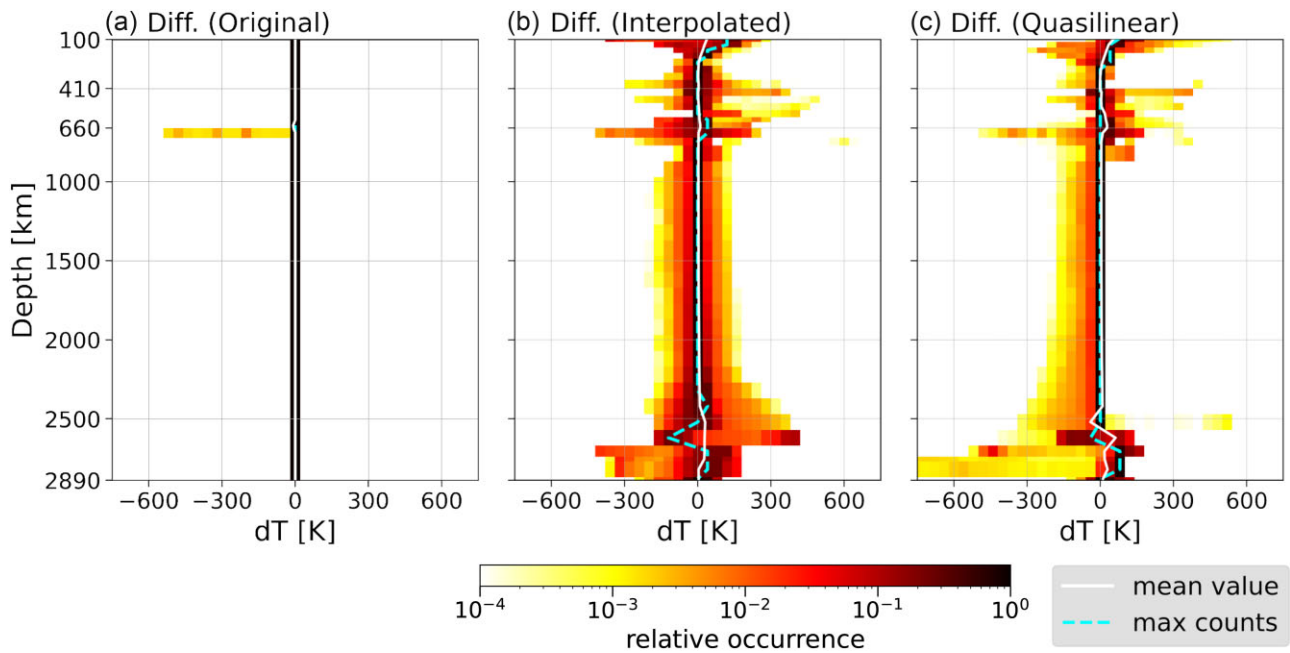


Figure 5. Depth-dependent histograms of the errors in the recovered temperature fields in the idealized case of perfect seismic resolution, using (a) the original, (b) the interpolated and (c) the quasilinear mineralogical conversion. Errors are computed as point-by-point differences between reference and recovered models, same as in Fig. 4. Histograms are normalized as described in Fig. 2.

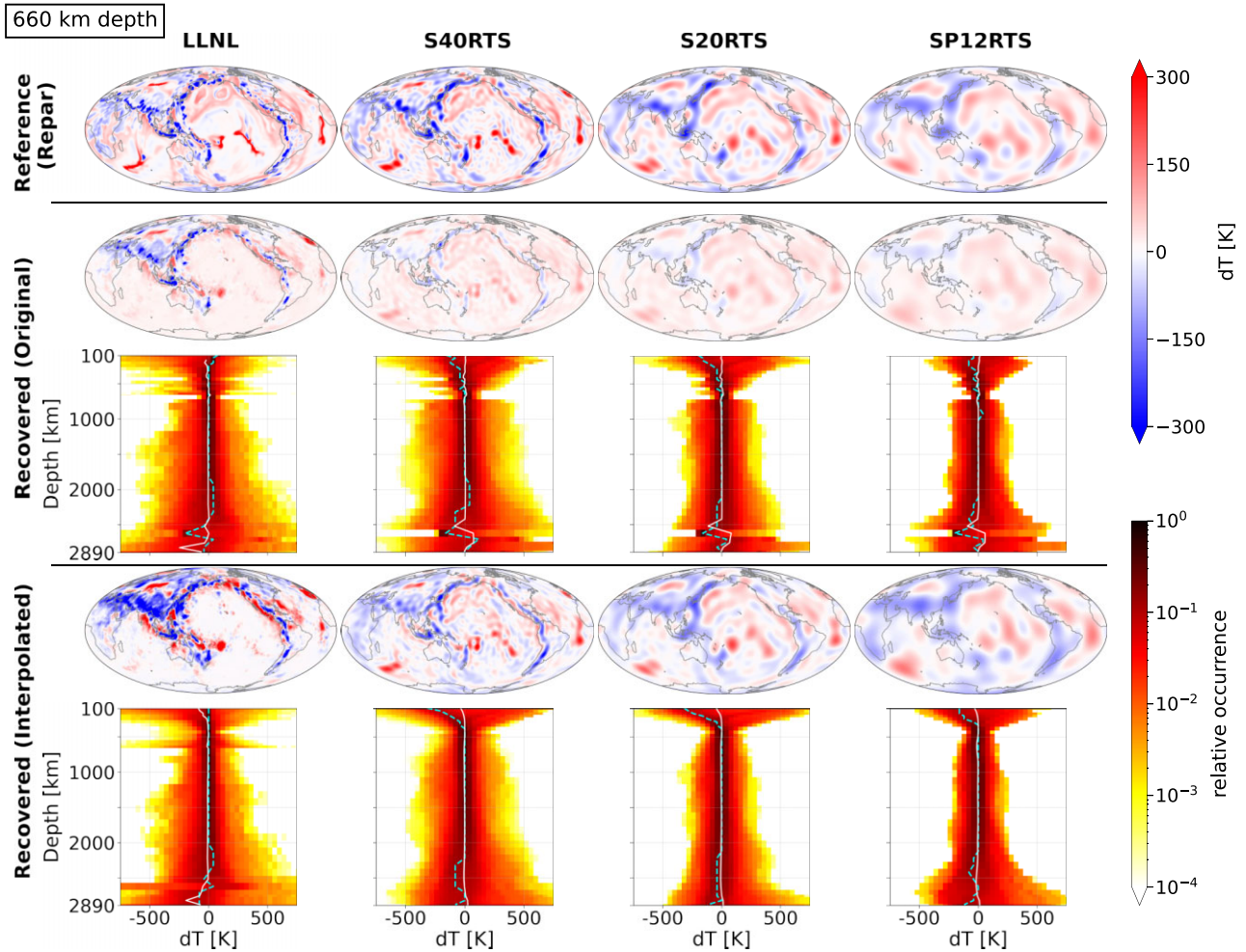


Figure 6. Reference and recovered temperature anomalies for the case of limited seismic resolution. (Uppermost row) Reparametrized temperature fields at 660 km depth that represent the reference for each tomographic filter. (Rows 2 & 4) Depth slices of recovered temperature anomalies after tomographic filtering with the resolution operator indicated above each column using (row 2) the original and (row 4) the interpolated mineralogical inverse conversion. (Rows 3 & 5) Associated histograms of the recovered temperature anomalies for the two conversion methods. Histograms are normalized as described in Fig. 2. Note that for the LLNL-reparametrized and -filtered cases, the total amount of grid points per layer differs from the rest, with 40 962 points in layers between surface and 660 km depth, and 10 242 below 660 km.

‘imaged’ seismic heterogeneity back to temperature in this case. Without the addition of tomographic filtering (Section 3.1), the (‘true’) seismic structure contains large velocity variations, introduced through phase transitions (Fig. 2b). After tomographic filtering, this heterogeneity is largely removed from the seismic image (Fig. 2c). Again, we map seismic velocities back to temperatures using all three conversion methods, and evaluate the recovered models in terms of depth slices and histograms (Fig. 6). This time, we show the full recovered temperature distributions instead of the errors to allow for an easy discrimination between over- and underestimated amplitudes. As pointed out in Section 2.1, we chose to exclude the non-physical reparametrization effects from the results for this more realistic scenario and use the reparametrized temperature fields as reference model. Note that the reference therefore changes for each tomographic filter, depicted in the top row of the figure.

Reparametrization alone introduces an artificial low-pass filtering effect (see e.g. Schubert *et al.* 2009b). This is best observed in the continuously increased smoothing and damping of structures between the S40RTS and SP12RTS parametrizations shown in Fig. 6. The range of recovered temperature anomalies (i.e. width

of the histograms) is further reduced after tomographic filtering, as expected. Deviations between the different filters highlight the unique resolving capabilities of the respective tomographic models. The choice of conversion approach is again most relevant in the vicinity of phase transitions, most prominently at the 660, which is chosen as the map depth in the figure. The systematics of the results using either of the two approximate mineralogies (interpolated or quasilinear) are very similar when tomographic filtering is included. We therefore focus on the interpolated case here.

Using the original mineralogical table on tomographically filtered seismic velocities for the conversion to temperature causes a systematic underestimation of the strength of thermal heterogeneity in regions of phase changes. In this case, the inverse mapping requires only small temperature perturbations to account for the damped seismic anomalies in combination with the high temperature-sensitivities of the original mineralogy. With the interpolated approach on the other hand, the reference temperatures are recovered more accurately at these depths, because the loss of complexity and associated lower T -sensitivity of v_s in this approximate mineralogy counteract the damping of the seismic structure.

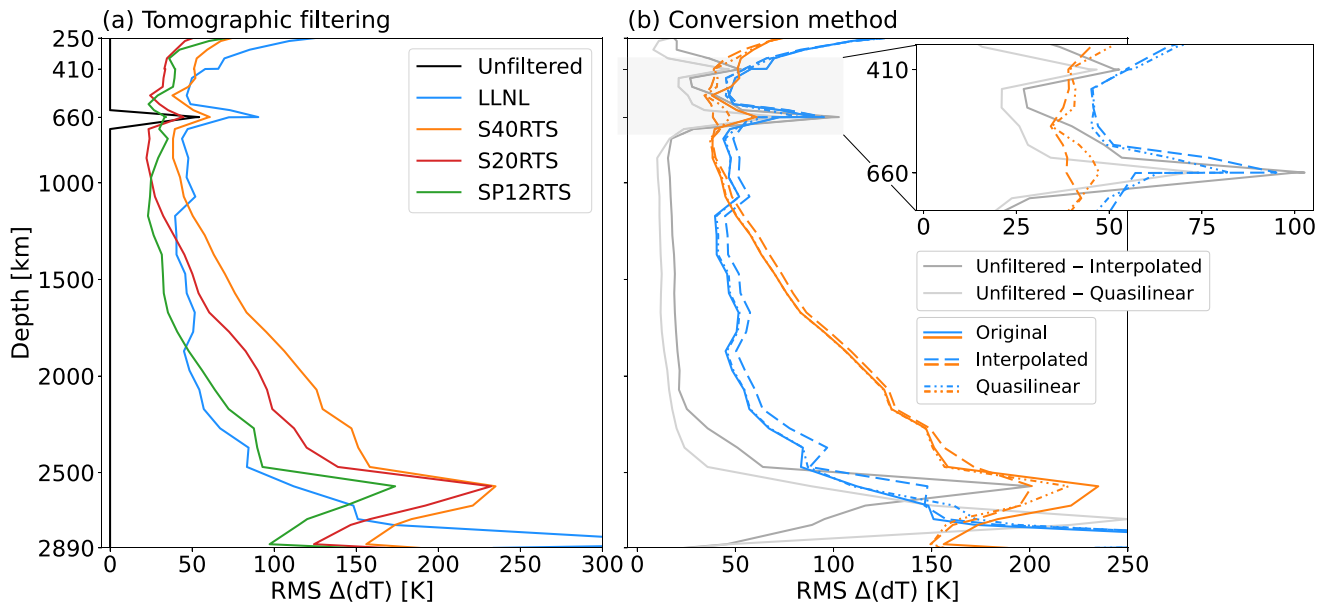


Figure 7. RMS-profiles of the differences between reference and recovered temperature anomalies. (a) Comparison of the effects of the four tomographic filters and the unfiltered (‘perfect resolution’) case using the original mineralogical inverse conversion. (b) Comparison of the different conversion methods for tomographic filters LLNL and S40RTS. The inset panel in (b) highlights the upper mantle transition zone. In this blow-up, solid lines belonging to the two filtered models together with the original mineralogy are omitted for clarity.

An exception to this behaviour is illustrated by model LLNL, which additionally inverts for discontinuity topography. As a result, seismic variations in the TZ are reduced less compared to the other tomographic filters. Interestingly, the ‘imaged’ seismic amplitudes in this case are too large, and do not sufficiently balance the lowered temperature-sensitivities inherent to the simplified mineralogy. Converting seismic anomalies that are close enough in amplitude to the ‘true’ values (i.e. more Earth-like) in consequence leads to overestimated temperatures with the interpolated (and also quasilinear; not shown) method, but to less severe underestimation with the original mineralogy.

In Fig. 7, the results after tomographic filtering are further summarized as root-mean-square (RMS) depth profiles of the differences between the reference for each filter and the respective recovered temperature fields. Panel (a) compares the results for all tomographic filters, using only the original inverse conversion. Average errors lie between 50 and 200 K for all tomographic filters applied. Clear peaks in the RMS-error exist at the 660 and at the pPv-transition, due to systematic underestimation of temperature anomalies, but less so for the 410. When adding the two other mineralogical conversion approaches as a second parameter (Fig. 7b), we restrict the comparison to the tomographic filters LLNL and S40RTS, which are most comparable in terms of their resolved scales and amplitudes. Since the models of the S++RTS-series are inherently constructed similarly, their results follow comparable trends and are well summarized by one of the filters. The same philosophy will be followed in the remainder of this study. Overall, the differences between the three mineralogical conversion methods are small compared to the effects of tomographic filtering. In the vicinity of phase transitions, the choice of conversion method is becoming more relevant, as seen before in Fig. 6. For S40RTS, the interpolated or quasilinear method outperform conversion with the original mineralogy at the 660. Using the interpolated table in particular with this tomographic filter, there is no prominent contribution to the RMS-error from mineralogical uncertainties beyond

the statistical effects of tomographic filtering alone (compared to the distinct peak at the 660 with the original conversion). With model LLNL on the other hand, such an effect is not observable, and the original conversion method performs equally or better at almost all depths.

3.3 Uncertain anelastic correction

In the following, we include the uncertainties related to mineral anelasticity. In our synthetic setup, it is possible to apply the anelastic correction individually to both the forward mineralogical mapping (which affects the ‘true’ mantle structure) and to the inverse mineralogical mapping, which represents the common assumptions in practice when interpreting seismic tomography. This allows us to test the influence of incomplete knowledge of mineralogical parameters and associated ‘wrong’ assumptions on the magnitude of the anelastic correction—while still having complete control and full knowledge about the underlying (‘true’) reference state. For simplicity, we restrict ourselves to two basic cases: overestimation or underestimation of the ‘true’ anelastic effects, as previously described in Section 2.3. To isolate the associated errors, we first show results without tomographic filtering in Fig. 8.

Anelasticity reduces seismic velocities, with exponentially growing effect with increasing temperature. Under- or overcompensating for this velocity reduction when using the original mineralogical data shifts the mean of the recovered temperatures by about 100–150 K. This is because the original inverse mapping converts absolute seismic velocities to absolute temperatures, which are directly affected by the miscompensated nonlinear velocity reduction. Underestimating the anelastic correction generally shifts recovered absolute temperatures towards higher values, which appear as strictly negative differences in the error histograms, while overestimating the correction has the opposite effect. In comparison, using either of the two approximate mineralogical models

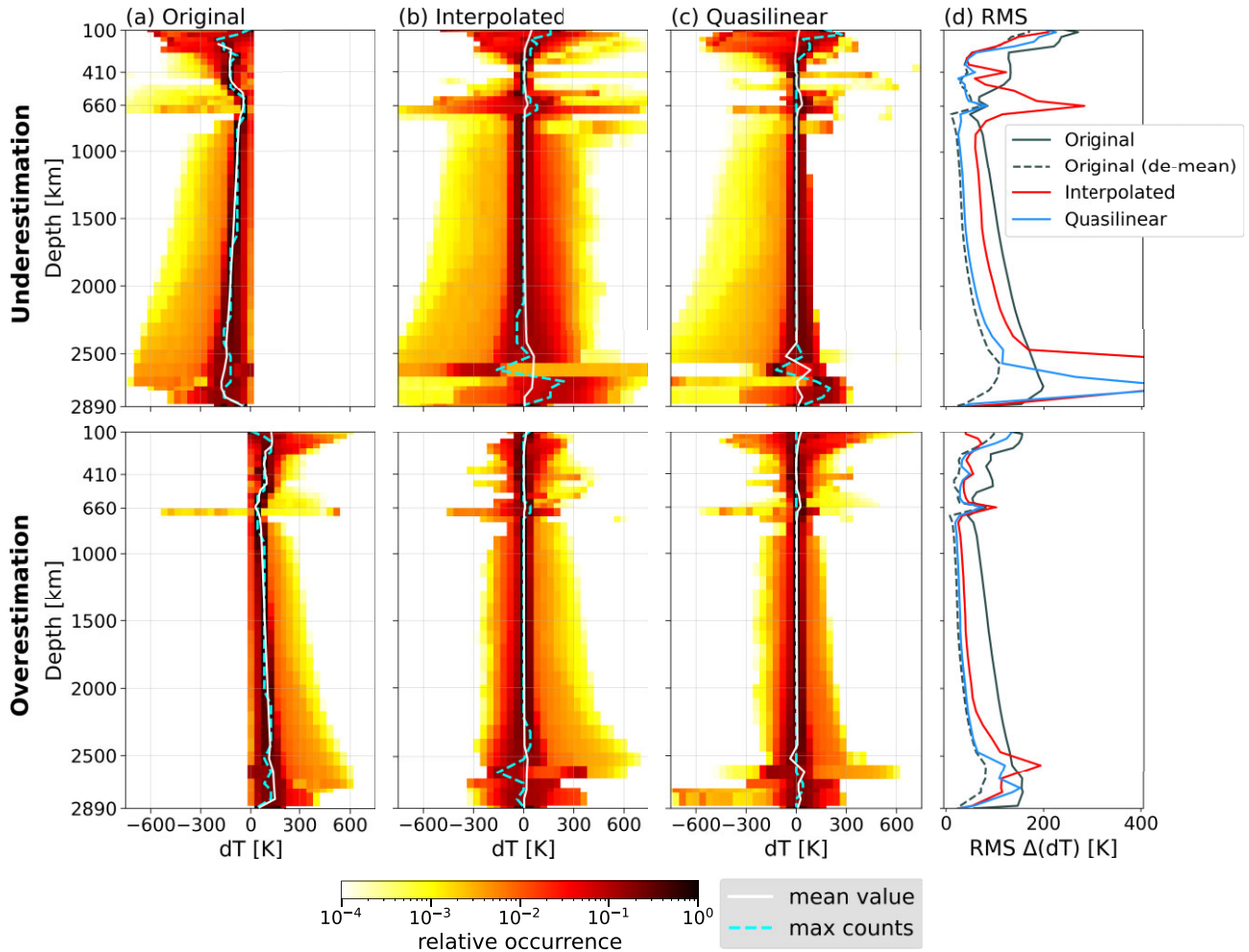


Figure 8. Effects of uncertainties in mineral anelasticity illustrated for two end-member scenarios: the anelastic correction applied to the mineralogical model is (top row) underestimated or (bottom row) overestimated. (a–c) Depth-dependent histograms of the errors in the recovered temperature fields in the idealized case of perfect seismic resolution, using (a) the original, (b) the interpolated and (c) the quasilinear mineralogical conversion. Errors are computed as point-by-point differences between reference and recovered models. The histograms are normalized as described in Fig. 2. (d) The respective average (RMS-)errors for each of the cases. For the original mineralogy, the errors are shown (solid line) with and (dashed line) without the shift of the mean included, illustrating the errors in absolute temperatures or temperature perturbations, respectively. The relevance of using the latter is discussed in Section 4.2. For details on how the anelastic correction is applied in the two scenarios, see Section 2.3.

preserves average temperatures, because both methods convert between relative variations directly. A strong asymmetry in the error histograms exists also for the approximate mineralogies, however, because the strong nonlinear temperature-dependence of anelasticity causes the modelled seismic velocities to not be uniformly affected by the anelastic correction. For all mineralogical conversion methods, underestimating the anelastic effects generally leads to inflated amplitudes of thermal anomalies and broader histograms, while too small temperature variations and narrow histograms result from overestimating the anelastic effects. The latter case however yields lower average errors for all conversion methods, particularly pronounced with the approximate mineralogies (compare top and bottom panels of Fig. 8d).

With tomographic filtering included (Fig. 9), the same general conclusions can be drawn. The differences between the respective variants are however less prominent with damped seismic model heterogeneity, as expected, especially for S40RTS. Still, overestimating the anelastic correction generally improves the RMS-misfit compared to the case of underestimated anelastic effects, as it limits

large deviations around phase transitions and overall reduces the dependence on the employed conversion strategy.

3.4 Uncertain bulk composition

Up to this point, we assumed that the mantle is well represented by an equilibrated pyrolitic composition (Davies *et al.* 2012; Zhang *et al.* 2013). However, through subduction of basaltic oceanic crust, chemically distinct material is constantly transported into the upper (and perhaps lower) mantle. Chemical diffusion and mechanical stirring are possibly too slow to effectively rehomogenize the mantle (Farber *et al.* 1994; Kellogg *et al.* 2002). Unequilibrated mechanical mixtures therefore are a common alternative to represent mantle composition (e.g. Hofmann & Hart 1978; Christensen & Hofmann 1994). We investigate scenarios of a deviation of the ‘true’ bulk composition from the assumption of pyrolite at thermodynamic equilibrium. For simplicity, we only vary bulk composition, because the inclusion of chemical heterogeneity inevitably raises the

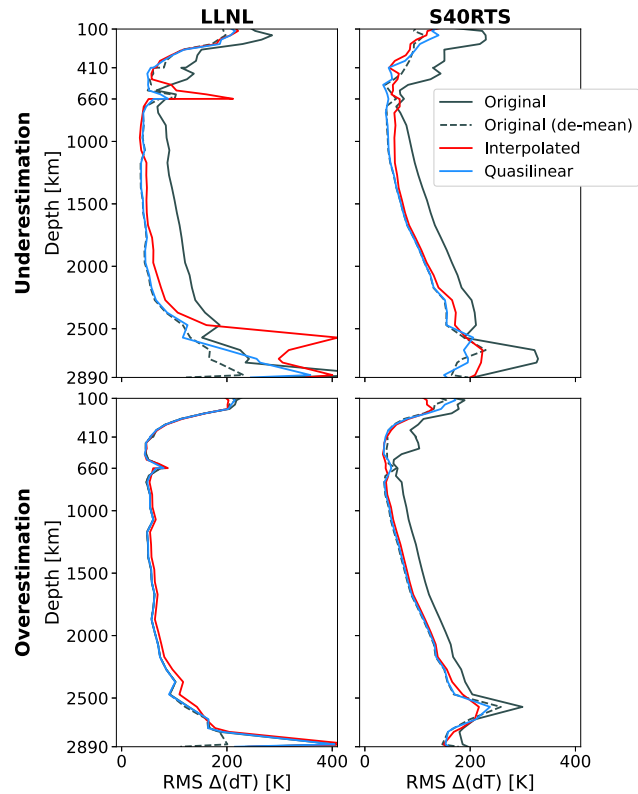


Figure 9. RMS-profiles of the differences between reference and recovered temperature fields with uncertain anelasticity and including the effects of tomographic filtering for models LLNL and S40RTS. Uncertainties in anelasticity are incorporated by mimicking (top) an underestimation or (bottom) an overestimation of the anelastic correction in the inverse mineralogical conversion. For the original mineralogy, we again plot the curves for two cases: (solid lines) with and (dashed lines) without the shift of mean values included (see also Fig. 8 for more details).

question to what extent the observed variations in seismic velocities are of thermal and compositional origin (e.g. Deschamps & Trampert 2003), resulting in non-unique interpretations. We test two cases with altered ‘true’ composition: (1) a mechanical mixing model (MM18), and (2) the extreme-case of a purely basaltic upper mantle. MM18 is composed of a mixture of 18 per cent basalt (bulk oceanic crust, BOC) and harzburgite (depleted mantle, DM) (Xu *et al.* 2008). The respective oxide proportions are listed in table C1, a more detailed description of the compositions and associated mineralogical models is given in Papanagnou *et al.* (2022). For the inverse conversion of seismic velocities to temperature, we always use equilibrium pyrolite, as this is the most commonly used assumption in such studies.

Results for a mismatch of bulk composition between forward and inverse mineralogical mapping are displayed in Fig. 10. For the original conversion, we distinguish between the errors in absolute temperatures (including potential shift of mean temperature) and the errors in relative variations (de-meaned). Differences between the reference and recovered temperatures for both composition scenarios are by far largest for absolute temperatures with the original conversion method. These compositional errors also dominate over the influence of tomographic filtering. Large deviations, well above 400 K on average, arise directly from compositional inconsistencies at the 660 for MM18, and in broader depth regions near the 410 and 660 for the basaltic composition. The latter is expected, given the

vastly different stability field of olivine minerals in a hypothetical basaltic mantle (Chemia *et al.* 2015; Chust *et al.* 2017). In comparison to the original method, the misfit in the TZ is strongly reduced with the interpolated or quasilinear conversion. With MM18 as the ‘true’ composition, the choice of conversion method furthermore affects the errors outside of phase changes in the unfiltered case, but not so much when tomographic filtering is applied. In the extreme-case of a basaltic upper mantle, the errors with both tomographic filters and in the unfiltered case are much smaller when converting with the approximated mineralogies instead of the original tables, for almost all depths shown. The same applies to the de-meaned original case, which yields similar results throughout the analysed depth range. Overall, deviations in bulk composition strongly restrict the recoverability of absolute temperatures in regions of phase transitions and potentially outweigh the effects of tomographic filtering, particularly with the original mineralogical data.

4 DISCUSSION

We have tested three different variants of the underlying mineralogical information for the conversion from seismic velocities to temperatures, with fundamentally different outcomes. Although one would intuitively expect the original inverse mapping to be most favourable, as it adequately represents the Earth’s complex mineralogy, our study shows that it is not so clear overall which of the conversion approaches yields the best results. This primarily depends on the characteristics of the tomographic model and, more generally speaking, the overall achievable seismic resolution.

4.1 Interplay between tomographic resolution and mineralogical complexity

The complexities inherent to the different mineralogical representations employed in this study primarily differ in regions of phase transitions. There, strong non-linearities exist in the $T-v_s$ relation of the original mineralogy, whereas seismic velocities in the two simplified mineralogical models show strongly reduced temperature-sensitivity (Fig. 3). Based on these discrepancies, we found that the benefit of using the complex, original mineralogy or rather taking advantage of a simplified, approximated version primarily depends on the resolving capabilities of the tomographic model.

In the ideal case of perfect resolution (i.e. without tomographic filtering; seismic velocity variations have realistic amplitudes), and without considering additional uncertainties, conversion with the original mineralogy expectedly outperforms its alternatives (Fig. 5). In this case, the ‘inverse’ mineralogy includes the complexities of the assumed true mineralogical behaviour. When converted with the approximate mineralogical models on the other hand, large seismic anomalies due to phase changes require overestimated thermal variations in the absence of the necessary mineralogical complexity. However, to be representative of realistic applications, limited tomographic resolution and its influence on amplitudes and spatial scales of the imaged seismic structure need to be considered. Once such effects are reproduced in the closed-loop experiment through tomographic filtering of the ‘true’ seismic structure, none of the conversion methods stand out as a universal best choice. Most notably, we find intriguing interactions between damped tomographic amplitudes and the different mineralogical adaptations. Then, using the original mineralogy to convert the damped seismic structure results in systematically underpredicted temperature perturbations

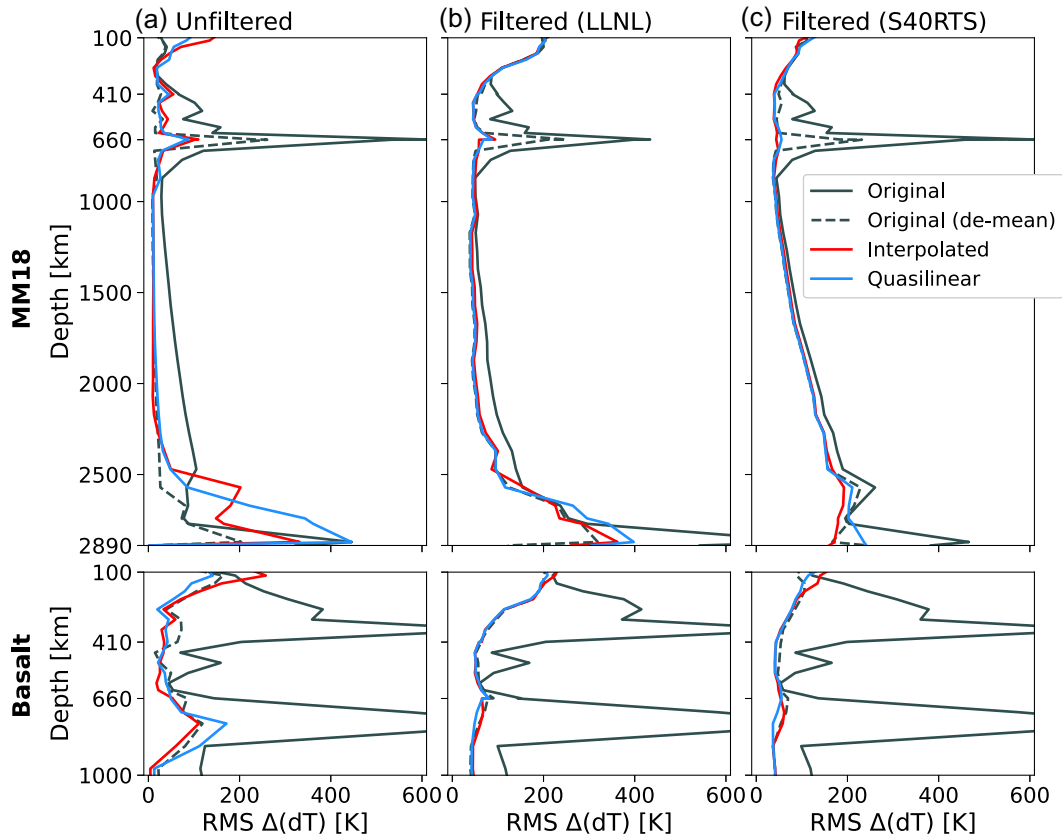


Figure 10. RMS-profiles of the misfit between reference and recovered temperature fields in case of inconsistent chemical composition in forward and inverse mineralogical conversion using the original, interpolated and quasilinear mineralogical representations. The mineralogical forward conversion incorporates either (top) a mechanical mixture (MM18) or (bottom) a basaltic composition. For the inverse conversion from seismic velocities to temperature, a pyrolitic composition is assumed in both cases, thereby mimicking the scenario that the ‘true’ bulk composition is different to the (commonly assumed) pyrolite. RMS-profiles are shown for (a) the idealized perfect-resolution case without tomographic filtering as well as for two tomographically filtered cases with (b) the LLNL and (c) the S40RTS resolution operator. For inverse conversion with the original mineralogy, we again show the errors with the shift of mean values (solid line) included or (dashed line) removed (see Fig. 8).

in the vicinity of phase transitions (Fig. 6). The magnitude of this effect ultimately depends on the degree of amplitude reduction in the respective tomographic model. With the four tomographic filters tested in this study, our results with the original mineralogy show that the thermal heterogeneity around the 660 is largely lost even for the (comparatively) high-resolution model S40RTS and only begins to be recoverable for model LLNL. With both the interpolated and quasilinear approximations, the associated lowered temperature-sensitivity around phase transitions counteracts the effects of reduced seismic amplitudes to some extent. Again, however, the quality of recovery is predominantly controlled by the amplitude loss due to filtering, and therefore the tomographic model itself. Put differently, if the amplitude reduction at depths of relevant phase transitions is not strong enough in the tomography, the interpolated or quasilinear approaches result in overestimated temperature variations, similar to the idealized case without tomographic filtering. For example, using the tomographic filter LLNL reduces average v_s -perturbations at the 660 by only 32 per cent with respect to the reparametrized reference, in comparison with 66, 65 and 57 per cent for S40RTS, S20RTS and SP12RTS, respectively. Converting the LLNL-filtered amplitudes back to temperature with the interpolated mineralogy yields largely overpredicted thermal anomalies (leftmost column in Fig. 6) and—in RMS-sense—does not offer an

improvement over the original conversion approach (Fig. 7b). With the other tomographic filters, using either the interpolated or quasilinear conversion reduces the RMS-errors compared to the original mineralogy (shown for S40RTS in Fig. 7b), as seismic anomalies are more strongly damped in depths of phase transitions.

In summary, the resolution characteristics of a tomographic model should be considered for the choice of mineralogical inverse mapping approach as follows:

(i) If perfect seismic resolution were possible, the original mineralogy would naturally perform best. With this inverse conversion, strong and short-scale variations in seismic velocities in the ‘true’ model, which result from combining a smooth temperature field with a complex forward mineralogy, can be mapped back to a smooth temperature field. Difficulties with the original mineralogy only arise at the 660, where the inverse mineralogical mapping is non-unique.

(ii) In the realistic case of limited tomographic resolution, the ability of the original mineralogy to recover the reference temperature field declines the stronger the damping of seismic amplitudes (i.e. with decreasing resolution; the larger the minimum structural length scales resolved in the tomography).

(iii) Approximations to the original mineralogy, such as an interpolated fit or a (quasi-)linearization, represent viable alternatives and, depending on the tomography of interest, may represent the better choice. With the imperfect resolution inherent to any tomographic inversion, the ‘imaged’ seismic velocities are smoother and damped in amplitude compared to the ‘true’ structure. When using the original mineralogy for the inverse conversion, the recovered temperatures then are rather rough and significantly underestimated in regions of phase transitions. The ‘imperfect’ approximate mineralogies partly mitigate this effect and produce smoother (and thus seemingly more realistic) temperature variations.

4.2 Absolute versus relative velocities/temperatures

When choosing between the different mineralogical mapping options, one also needs to consider possible advantages and disadvantages of either converting absolute seismic velocities to absolute temperatures (original), or alternatively converting directly between relative variations (interpolated/quasilinear). The information contained in the original mineralogy depends on absolute seismic velocities, which potentially bears a considerable drawback: in standard traveltimes tomographies, seismic velocities are usually expressed as perturbations with respect to a 1-D seismic reference profile, often PREM (Dziewoński & Anderson 1981) or AK135 (Kennett *et al.* 1995). However, it has been noted that radial seismic models cannot reflect the mantle’s average physical structure, due to biases when averaging over 3-D topographic variations of phase transitions (Styles *et al.* 2011) and potential 3-D chemical heterogeneity (Cobden *et al.* 2008). Additionally, seismic profiles derived from body-wave traveltimes are likely shifted towards faster velocities overall, because the majority of earthquakes occur in and around subduction zones (e.g. Nolet *et al.* 1994; Davies & Bunge 2001). Absolute seismic velocities from tomographic models are therefore difficult to interpret thermally, because uncertainties in the 1-D reference directly propagate into the derived absolute temperatures. This effect is mitigated when using tomographic models obtained with full-waveform inversion, as they iteratively update absolute seismic velocities directly (e.g. Fichtner *et al.* 2013; Bozdağ *et al.* 2016; Thrastarson *et al.* 2022; Cui *et al.* 2024); not considering their ambiguous dependence on the starting model (Virieux & Operto 2009).

With the interpolated approximation on the other hand, the exponential fit to absolute seismic velocities is tied to a radial reference. This causes the inverse conversion to be effectively independent of the assumed seismic 1-D profile, as long as the one used to derive the exponential fit is the same as the one underlying the tomographic model. The quasilinear approach is truly independent of a radial reference and converts between relative variations directly. Using either of the two options thus minimizes the dependence on accurate seismic reference profiles, but consequently limits direct interpretability of seismic data to temperature deviations. In this case, absolute temperatures can only be assessed by linking the variations to a 1-D temperature profile. Such profiles, often simply taken to be adiabats (e.g. Brown & Shankland 1981; Katsura 2022), to date have yet to be successfully matched with radial seismic profiles using mineralogical constraints (Cammarano *et al.* 2005; Cobden *et al.* 2008, 2009).

Beyond mineralogical and tomographic limitations, one advantage of converting between relative rather than absolute perturbations is that it preserves average temperatures, for example under the

influence of the uncertain anelastic correction (Fig. 8), and considerably reduces sensitivity to variations in bulk composition (Fig. 10). Cammarano *et al.* (2003) stated that, due to the nonlinear dependence of anelasticity to temperature, relative velocity variations cannot directly be interpreted. However, both relative conversion methods we employ in this study are derived from the anelastically corrected $T-v_s$ relation of the original mineralogy, and thus intrinsically account for the temperature-dependence of anelastic effects. Additionally, this conclusion of Cammarano *et al.* (2003) does not account for limited tomographic resolution, which renders a thermal interpretation of seismic velocities imperfect in any case. As displayed in Figs 8 and 9, converting absolute or relative seismic velocities does not crucially alter the ability to recover correct temperatures under the influence of uncertain anelasticity. In both figures, we show two versions of RMS-errors for the original mineralogy: one for the ‘full’ error in absolute temperature (solid line), and one with the mean removed before RMS-calculation to obtain the error of the associated temperature variations (de-meaned; dashed line). For absolute temperatures, the comparatively large RMS-deviations with the original mineralogy are strongly affected by the associated shift of the mean values away from zero. When compared in terms of relative variations, however, the original mineralogy generally produces better results than the two approximations. Depending on the requirements of the problem, either of the two representations might be appropriate for the estimation of associated uncertainties. An example of this, regarding the treatment of compressibility in geodynamic models, is further discussed in Section 4.3.

4.3 Implications for geodynamic modelling

A major motivation of our work is to provide quantitative error estimates for geodynamic studies that rely on temperatures derived from tomography. Geodynamic inverse models, in particular, aim at reconstructing the evolution of mantle flow in the past (e.g. Colli *et al.* 2018; Ghelichkhan *et al.* 2021). In these so-called ‘retrodictions’, mantle flow in the Cenozoic is constrained by the physics of fluid dynamics and an estimate of the present-day temperature distribution in the mantle, which serves as a starting point for a time-reversed simulation (technically speaking, however, this is the ‘final’ or ‘terminal’ state in accordance with the physical direction of time). Here, we have quantified several different contributions to the errors that inherently occur when deriving those temperatures from tomographic models. To assess the influence of temperature-errors on the retrodictions, driven by the associated buoyancy forces, it is important to also understand the seismic observations in terms of the associated density structure. Classically, convection simulations for a compressible mantle are formulated using the ‘Truncated Anelastic Liquid Approximation’ (TALA; Jarvis & McKenzie 1980), which linearizes the buoyancy effects around a radial reference density profile based on the local temperature deviations and the thermal expansivity of the material. First-order effects of a mismatched final state on the evolution of mantle flow reconstructions with TALA were previously assessed by Colli *et al.* (2020), with the effects of seismic resolution approximated by simple low-pass filtering (i.e. not taking into account the laterally and radially varying effects of uneven data coverage). In the absence of short-wavelength features, they found in particular that small-scale artefacts in the thermal boundary layers of the reconstructed initial state emerge to counteract the model-driven development of short-wavelength anomalies.

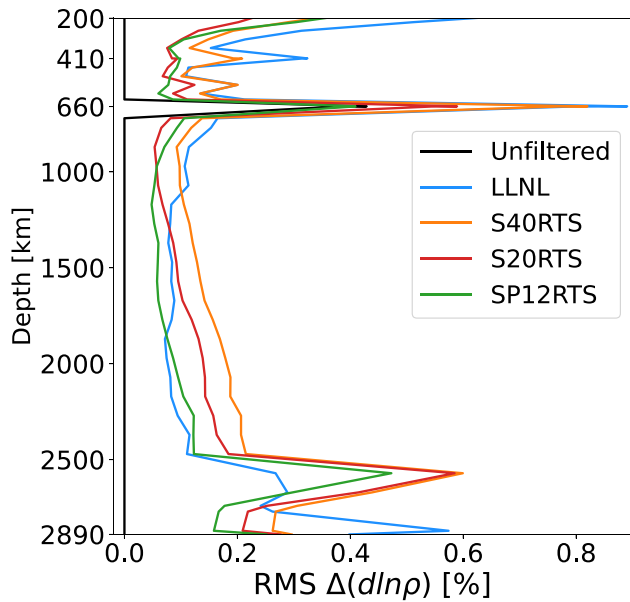


Figure 11. RMS-profiles of the errors in recovered density anomalies for the unfiltered perfect-resolution case and for the four different tomographic filters. The seismic anomalies were converted to density through temperature using the original mineralogical table. Compare with Fig. 7(a) for the different behaviour of the errors in recovering temperatures versus density.

A more physically complete treatment of compressibility has recently been introduced in the form of the ‘Projected Density Approximation’ (PDA; Gassmüller *et al.* 2020, who present a detailed overview on different formulations of compressibility in geodynamic simulations). The PDA is based on tabulated material properties from thermodynamic mineralogical models, which capture physical non-linearities in a self-consistent fashion, as discussed in detail before. With pressure and temperature as input, the associated space- and time-dependent density structure can be extracted consistently from the lookup-tables at each time step. This way, buoyancy effects in particular of phase transitions should be captured correctly in the mantle flow simulation.

In order to use tomographic models as a constraint on buoyancy in geodynamic inverse models that employ the PDA, present-day densities need to be determined from the observed seismic velocities via the inferred absolute temperatures. Knowledge of the temperature distribution is necessary, because just like with TALA, the underlying equations are solved for temperature (or entropy; Dannberg *et al.* 2022), and not density. Errors in the estimated temperature field thus directly propagate into the driving buoyancy forces, but can be modulated by the choice of mineralogical inverse mapping (see Section 4.1). A logical choice would be to derive the present-day temperatures by conversion with the original mineralogical tables, physically consistent with the determination of material properties from temperature and pressure at model runtime. This approach can be additionally motivated by the PDA’s requirement of absolute temperatures, which again favours the original method (discussed in Section 4.2). The associated errors in density for this case are shown in Fig. 11. Compared with the results in temperature (Fig. 7a), the density misfit is even more pronounced at phase transitions, particularly at the 660 and the pPv-transition. This is because deviations in temperature cause a portion of the model to be associated with the wrong mineral phase, which then strongly affects the density estimate. At the 660, the average density error

reaches values close to 1 percent, which is on the order of the expected density anomaly of thermal mantle plumes itself (given typical estimates of plume excess temperature; e.g. Albers & Christensen 1996; Bunge 2005; Leng & Zhong 2008). For comparison, the RMS density variations of the reference MCM are 0.97 per cent at the 660 and 0.81 per cent at 2600 km. It must, however, be noted that the RMS-metric is sensitive to the smallest scales, while mantle convection is driven by large-scale buoyancies (Colli *et al.* 2020).

Alternatively, one could attempt to mitigate large density errors by initially deriving the temperature distribution with the interpolated or quasilinear mineralogy and subsequent translation of the temperature variations to density anomalies together with an (uncertain) reference temperature profile. As discussed in Section 4.1, results in this case depend on an adequate fit between approximate mineralogy and tomographic resolution, as it would otherwise lead to systematically mismatched temperatures, and consequently densities.

Dynamically, if the PDA is employed in geodynamic inverse models, important implications could arise from the ambiguous influence of the 660 phase transition on vertical mass exchange between upper and lower mantle. The ringwoodite transition mainly associated with the 660 discontinuity is endothermic, generally tending to impede vertical flow. Complications are caused by two additional phase transitions, which have been identified at a similar depth, potentially becoming dominant at colder (akimotoite + ferropericlasite = stishovite) or hotter (garnet = bridgmanite) temperatures (see Hirose 2002; Jenkins *et al.* 2016; Papanagnou *et al.* 2022). Both of those phase transformations are exothermic, therefore supporting vertical mantle flow, rather than hindering it. In case of wrong temperatures in the terminal state (i.e. at the start of the geodynamic inversion), it is therefore likely that different phase transitions, implicitly defined by the mineralogical model, are ‘activated’ during the model’s evolution, erroneously switching from an endothermic to an exothermic regime (or vice versa) and consequently altering or even flipping large-scale buoyancy forces in the geodynamic system. Fig. 12 displays potential differences of the distribution of dominant phase transitions in the present-day state, determined by the derived temperatures. It can be seen that in conjunction with different tomographic filters, the relative distribution between exothermic and endothermic transformations can considerably be modified, compared to the ‘true’ reference model. For instance, in the unfiltered case together with the interpolated mineralogy, the area of the exothermic garnet transition is greatly increased, potentially (artificially) emphasizing the ascent of hot plumes through the 660. On the other hand, using the original tables together with the LLNL-filter lessens the significance of the garnet transition, but at the same time locally increases the extent of the exothermic stishovite transition in slab regions around Asia. With the increased amplitude reduction from S40RTS, both extreme-temperature transitions largely disappear in favour of the endothermic ringwoodite transition, therefore reducing the overall buoyancy in the system (even more so for filters S20RTS and SP12RTS; not shown). Uncertainties in the anelastic correction and the corresponding shift in absolute temperatures using the original tables could exert a similarly strong control on the dominant phase transformations.

In light of these results, it is likely that errors in the final-state temperature distribution could critically alter the geometry of the convective system, potentially determining to what extent the 660 poses a hindrance to mantle convection in geodynamic inverse models that employ the PDA. Note again that errors in the present-day

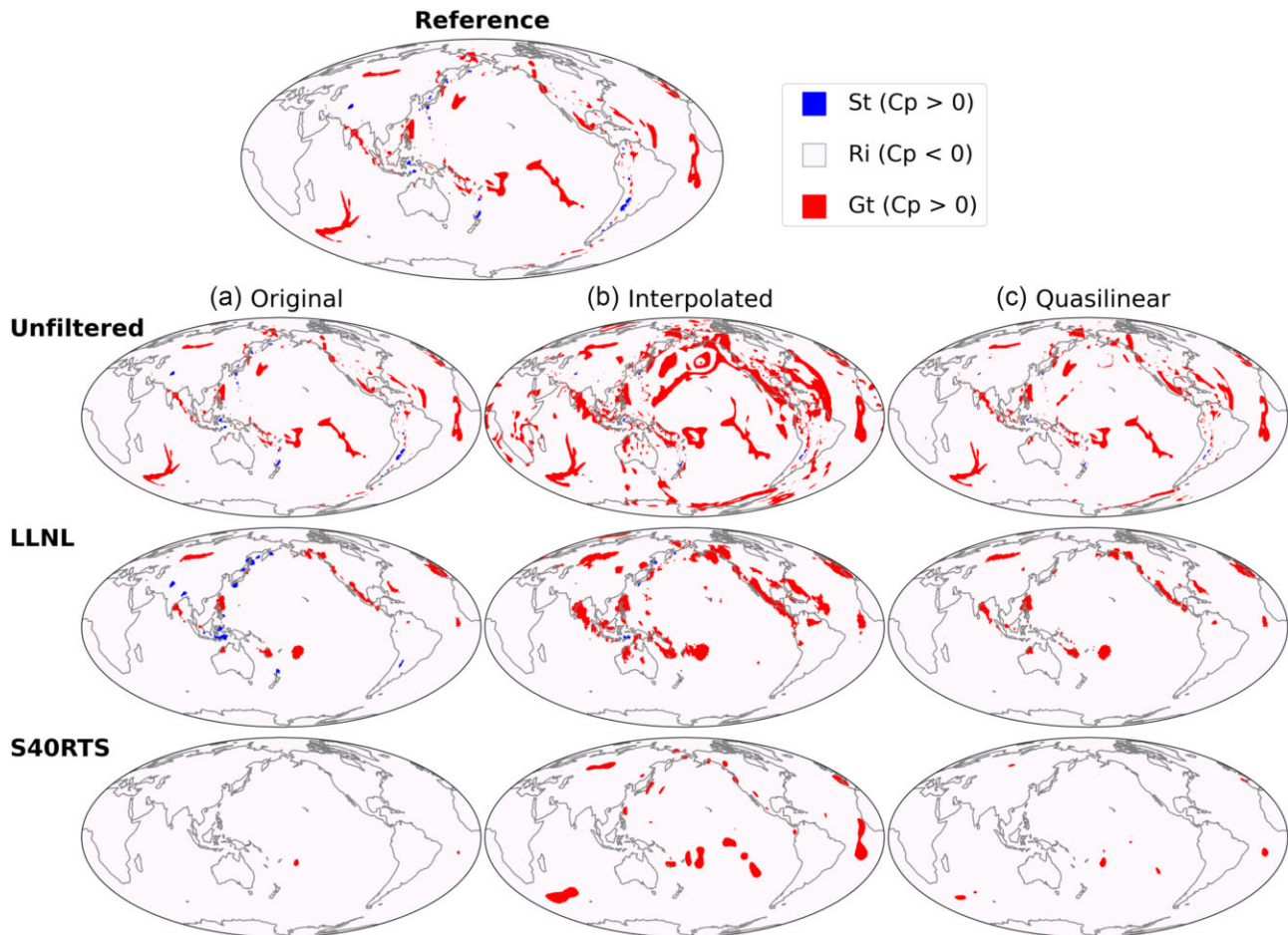


Figure 12. Maps of the laterally varying dominant phase transitions at the 660 associated with the recovered temperature fields using (a) the original, (b) the interpolated and (c) the quasilinear mineralogy, with and without tomographic filtering applied. Blue areas indicate the presence of the stishovite transition ($ak + fp = st$) for low temperatures ($T < 1200$ K), red areas indicate the presence of the garnet transition ($gt = br$) for high temperatures ($T > 2150$ K). The grey colour indicates occurrence of the ‘common’ ringwoodite transition ($ri = br + fp$) with temperatures in between 1200 and 2150 K. Dynamical relevance originates from the opposing Clapeyron slopes (C_p) of the three phase transformations: both the stishovite and garnet transition have positive Clapeyron slopes, supporting vertical mantle flow across the 660, whereas the Clapeyron slope of the ringwoodite transition is negative, potentially impeding vertical flow. The temperature ranges for the respective phase transitions are taken from Papanagnou *et al.* (2022). (Abbreviations: ak = akimotoite, br = bridgmanite, fp = ferropericlase, gt = garnet, ri = ringwoodite, st = stishovite.).

buoyancy structure can be partially controlled by careful selection of the method to derive temperature/density variations from tomography. Dynamic effects from misrepresented phase changes during model evolution are however a potential pitfall of the PDA in general, since they are modulated by (likely erroneous) absolute temperatures and not density. This is particularly relevant for the geodynamic retrodictions, because the chaotic nature of mantle convection might cause the errors in the present-day state to grow exponentially through model evolution. In geodynamic inverse simulations, such complications can presumably only be avoided with simpler formulations of compressibility, such as TALA, that do not dynamically include variable phase transformations. So, while the self-consistent incorporation of mineralogical constraints via the PDA constitutes a logical improvement towards Earth-like geodynamic simulations that run convection forward in time, it needs to be thoroughly investigated whether the same applies to geodynamic inverse models under the influence of systematic errors in the final state. More testing with PDA and TALA is required to create comparable flow evolutions and evaluate how a mismatched final

state could shape geodynamic inverse models with either of the two compressibility formulations.

The resulting density-errors found in this study similarly apply to instantaneous flow calculations (e.g. Simmons *et al.* 2006; Long & Becker 2010; Richards *et al.* 2020, 2023), which, for example, model convective flow velocities and the generation of anisotropy based on the present-day density structure derived from seismic tomography. Contrary to the applications to (forward or inverse) MCMs, no association between densities and temperatures is needed in that case, thus relieving the requirements on how to derive the density structure from tomographic models. For instance, uncertainties from temperature-dependent phase transitions could entirely be avoided by converting the observed seismic velocities directly to densities using linear scaling parameters (e.g. Simmons *et al.* 2009), analogous to the quasilinear approximation in this study. In any case, the errors occurring in single depth layers of relevant phase transitions likely only have a minor impact on the overall integrated buoyancy, and thus the results of the (one-step) instantaneous flow calculations.

4.4 Additional sources of uncertainty

In this study, we have quantified uncertainties relating to limited tomographic resolution, the mineralogical approximation, anelastic correction and bulk composition. In Section 4.2, we additionally outlined possible issues arising from uncertain seismic reference profiles, when converting absolute seismic velocities with the original mineralogical tables. Assessing further uncertainties that influence our understanding of the thermal structure of the mantle would in general be possible with our synthetic setup, but goes beyond the scope of this study. Further limitations we do not analyse here include:

(i) Chemical variations

Chemical heterogeneity is likely to exist to some extent in the mantle, owing to the constant subduction of chemically differentiated basaltic crust and harzburgitic lithosphere. Accounting for the possibility of chemical variations introduces a further non-uniqueness to the interpretation of seismic velocities, or alternatively requires independent data that allows to distinguish between thermal and chemical origins of velocity variations. On the other hand, a homogeneous pyrolite composition has been shown to adequately reproduce global traveltimes statistics (Schuberth *et al.* 2012), as well as seismic characteristics and rheology of the mantle in the TZ (e.g. Akaogi 2007; Frost 2008; Ishii *et al.* 2018) and lowermost mantle (e.g. Schuberth *et al.* 2009a, b; Davies *et al.* 2012; Koelemeijer *et al.* 2018). Additionally, at least in the upper mantle, seismic wave velocities are much more sensitive to temperature than composition (e.g. Sobolev *et al.* 1996; Deschamps *et al.* 2002; Cammarano *et al.* 2003; Lebedev *et al.* 2024), while composition becomes relevant only with increasing pressure (Trampert *et al.* 2001). Overall, the addition of chemical uncertainties likely plays no overarching role within the resolution lengths of seismic tomography. The assumption of an isochemical composition is therefore reasonable and allows to interpret the seismic structure uniquely in terms of temperature. Nevertheless, the quantified errors of this study likely constitute a lower bound of the overall uncertainties when interpreting tomographic models, and would only be further elevated with the addition of potential chemical heterogeneity.

(ii) Elastic and anelastic parameters

The uncertainties accompanying the elastic and anelastic parameters making up the mineralogical models are well explored and published, for example in the recent update to the database of Stixrude & Lithgow-Bertelloni (2024). Earlier studies have investigated these uncertainties and their influence on the ability to determine mantle properties from seismic models before (e.g. Connolly & Khan 2016). Cammarano *et al.* (2003) estimated that they introduce an ~ 250 K uncertainty on inferred temperatures in the shallow lower mantle. A large portion of this effect is expected to be caused by the anelastic uncertainty, which we cover in Section 3.3 (see also Schuberth & Bigalke 2021, for more details on the anelastic contribution to the temperature-derivatives of seismic velocities). We find average deviations between 100 and 150 K in the shallow lower mantle due to uncertain anelasticity, in general agreement with the estimate of Cammarano *et al.* (2003). However, since our assessment of the anelastic correction relies on two end-member scenarios, and mineralogical models have undoubtedly improved over the last 20 yr, the value of 250 K now very likely constitutes an upper limit to the influence of the combined elastic and anelastic uncertainty.

(iii) Reference temperature

Absolute temperatures in the mantle are poorly constrained. We have shown that the conversion of relative seismic variations to temperature can bear some advantages, because it reduces the sensitivity

to uncertainties in e.g. bulk composition or 1-D seismic velocity. In this case, however, interpretation of the results in terms of absolute temperatures is difficult and relies on an accurate 1-D temperature profile. This limits the usability of either of the two approximate mineralogies if absolute temperatures are required.

Another factor to consider is the mean temperature profile of the reference MCM in our closed-loop, and its interaction with potential non-bijective (i.e. non-unique) T - v_s relations in the original mineralogical data (see Section 2.2). Based on the simplest inversion procedure (parameters at each grid point are converted in isolation, independent of the observations at close radial or lateral neighbours), any seismic velocities falling into the non-bijective range (i.e. that could be explained by multiple temperatures) are translated to the suitable temperature closest to the mean model temperature at that depth. Temperature values further away from the mean within the non-unique range can never be reached with this scheme. This results in unrecoverable thermal perturbations between roughly -200 and -600 K at the 660, as seen in the associated deviations in Figs 4(a) and 5(a). The ‘width’ of this non-recoverable temperature band of ~ 400 K is fixed and corresponds to the non-bijective portion of the original mineralogy (along the thick red line in Fig. 3, between ca. 1500 and 1900 K). However, the fraction of model grid points affected depends crucially on the assumed mean temperature during parameter conversion. In our case, only about 2 per cent of the reference model temperatures fall into the non-bijective range between -200 and -600 K. This number potentially increases to about 6 per cent, if one considers an average temperature that is lower by 100 K, and to about 40 per cent with a 200 K decrease.

At the 660, absolute temperatures are comparatively well explored, due to the usability of the seismically visible discontinuity as a geothermometer (e.g. Ito & Takahashi 1989; Ritsema *et al.* 2009; Waszek *et al.* 2021; Katsura 2022). With 2035 K, our average MCM temperature at 660 km depth is about 50–150 K larger than the values found in the literature, indicating that the non-unique section of the original conversion might produce more significant deviations than shown in this study.

(iv) Tomographic uncertainty

Tomographic filtering accounts for limitations in resolution, but does not consider uncertainties in the tomographic model parameters themselves, related to the influence of seismic data errors from imperfect traveltimes determination, source localization, crustal correction, modelling errors, etc. Assessing uncertainties in large-scale tomographic models is computationally very expensive in the framework of traditional damped least-squares inversions, and thus is often disregarded (Zaroli 2016). So far, only a small number of studies have determined model covariances in an attempt to estimate uncertainties beyond resolution (e.g. Nolet *et al.* 1999; Zaroli *et al.* 2017; Simmons *et al.* 2019; Cui *et al.* 2024). Recently, Freissler *et al.* (2024) developed a scheme that allows to explicitly quantify both resolution lengths and tomographic model uncertainty based on the SOLA-Backus–Gilbert inversion scheme (Zaroli 2016), which explicitly provides specific control over the trade-off between these parameters at every grid-point. Such methodologies, applicable at global scale, will further help to improve our understanding of the state of the mantle.

5 CONCLUSION

Using a closed-loop synthetic experiment, with geodynamic, mineralogical and seismic modelling components, we systematically

tested the theoretical ability to derive robust estimates of mantle temperatures from tomographic models. We assessed the temperature distributions recovered from tomographic ‘images’ of a mantle circulation model, using different realizations of the underlying mineralogy: the original table as well as two approximate versions. In our analysis, we quantified the misfit between reference and recovered temperature field, with a specific focus on the influence of various mineralogical uncertainties in combination with the effects of limited seismic resolution. To obtain unique temperatures without including additional data, such as gravity/geoid measurements, seismic attenuation, or electrical conductivity, a negligible influence of lateral chemical heterogeneity was assumed. Our study shows that accurate inferences of the thermal mantle structure are primarily hampered by the limited resolving power of seismic tomography. In most cases, the choice of mineralogical conversion approach was found to only play a secondary role. The laterally averaged (RMS-) errors in the recovered temperature fields vary with depth, with values between 50 and 100 K in the upper mantle. For some tomographic filters, the errors increase with depth up to 200 K close to the core–mantle boundary. For comparison, the respective reference model’s average (RMS) strength of thermal heterogeneity increases from values on the order of 100 K in the upper mantle to about 250–300 K at 2500 km depth. Additional large systematic errors occur in the vicinity of phase transitions, so that the total error at those depths is comparable in magnitude to the reference model’s temperature variations. Overall, our results regarding the strategies to convert seismic velocities to temperature can be summarized as follows:

(i) The ‘better resolved’ the tomographic model (i.e. the more realistic the amplitudes of seismic heterogeneity and the finer the structures), the more important it is to account for the complexities in the mineralogy; that is, the original representation should be used. Approximated versions of the mineralogical model generally are more advantageous together with lower resolution tomographies.

(ii) Overestimating the anelastic correction to seismic velocities produces more reliable results with generally smaller average errors than if anelastic effects are underestimated. It could for real-world applications thus be advisable to choose the governing parameters such as to push the magnitude of the anelastic correction towards its upper bound. This is especially true when using the interpolated mineralogical conversion together with high-resolution tomographic models.

(iii) Converting relative seismic variations to temperature perturbations generally is more robust than the conversion of absolute seismic velocities to absolute temperatures, particularly under the influence of uncertainties in the anelastic correction and the incomplete knowledge on bulk composition.

(iv) Absolute temperatures can directly be derived with the original mineralogical inverse mapping, but are strongly affected by potential uncertainties in the anelastic correction, bulk composition or the seismic reference profile. With the approximated mineralogies, absolute temperatures can only be inferred as deviations from a (uncertain) reference mantle geotherm.

The errors in the recovered temperature distribution also impact the related densities and therefore have important implications for the associated buoyancy forces when employed in geodynamic inverse models. Modern formulations of compressibility in geodynamic simulations, which incorporate the temperature-dependent buoyancy effects of phase changes dynamically, (e.g. the ‘Projected Density Approximation’; Gassmöller *et al.* 2020), need to be treated with particular care in light of our findings. With these formulations,

incorrect temperature inferences could ‘activate’ the wrong phase transitions and potentially lead to a flip in sign of the associated Clapeyron slope. Large-scale buoyancy forces in the models could thus be altered or even reversed. Owing to the nonlinear nature of the convection equations, these initial errors are likely to further increase exponentially during model evolution. Thorough testing is required to assess the influence of different compressibility formulations on the accuracy of geodynamic retrodictions.

Most importantly, our analysis shows that thermal interpretations of tomographic models and their potential implications for simulations of mantle convection critically depend on the resolving capabilities of the specific tomography, as well as the confidence in the parameters underlying both seismic and mineralogical models. Methods to retrieve temperatures from tomographically imaged seismic velocities need to be selected carefully to make reliable deductions, at best with explicit knowledge about the tomographic model’s resolution characteristics in the form of a resolution operator or generalized inverse. This will become increasingly important with the upcoming generations of tomographic models that come along with improved resolution, including at depths of major phase transitions.

ACKNOWLEDGMENTS

We thank the editor Dr Tobias Keller, Juan Carlos Afonso and one anonymous reviewer for their constructive and helpful comments on the manuscript. We further thank Nathan A. Simmons, Jeroen Ritsema and Paula Koelemeijer for providing the resolution operators of their tomographic models as well as for sharing their tomographic filtering codes. Funding for this work was provided by the Deutsche Forschungsgemeinschaft (DFG, German Research Foundation) under grants SCHU 2914/5-1, SCHU 2914/5-2 and TH 1530/21-2. Computational infrastructure at the institute in Munich was funded by DFG - 518204048.

DATA AVAILABILITY

The data underlying this paper will be shared on reasonable request to the corresponding author.

REFERENCES

- Afonso, J.C., Fullea, J., Yang, Y., Connolly, J. A.D. & Jones, A.G., 2013. 3-D multi-observable probabilistic inversion for the compositional and thermal structure of the lithosphere and upper mantle. II: general methodology and resolution analysis, *J. Geophys. Res. Solid Earth*, **118**(4), 1650–1676.
- Afonso, J.C., Rawlinson, N., Yang, Y., Schutt, D.L., Jones, A.G., Fullea, J. & Griffin, W.L., 2016. 3-D multiobservable probabilistic inversion for the compositional and thermal structure of the lithosphere and upper mantle: III. Thermochemical tomography in the Western-Central U.S., *J. Geophys. Res. Solid Earth*, **121**(10), 7337–7370.
- Akaogi, M., 2007. Phase transitions of minerals in the transition zone and upper part of the lower mantle, in *Advances in High-Pressure Mineralogy*, Vol. 421, ed., Ohtani, E., Geological Society of America.
- Albers, M. & Christensen, U.R., 1996. The excess temperature of plumes rising from the core–mantle boundary, *Geophys. Res. Lett.*, **23**(24), 3567–3570.
- Becker, T.W. & Boschi, L., 2002. A comparison of tomographic and geodynamic mantle models, *Geochem. Geophys. Geosyst.*, **3**(1), doi:10.2919/2001gc000168.
- Becker, T.W., Kustowski, B. & Ekström, G., 2008. Radial seismic anisotropy as a constraint for upper mantle rheology, *Earth planet. Sci. Lett.*, **267**(1–2), 213–227.

- Bercovici, D., Schubert, G. & Tackley, P.J., 1993. On the penetration of the 660 km phase change by mantle downflows, *Geophys. Res. Lett.*, **20**(23), 2599–2602.
- Bina, C.R. & Helffrich, G., 1994. Phase transition Clapeyron slopes and transition zone seismic discontinuity topography, *J. Geophys. Res. Solid Earth*, **99**(B8), 15 853–15 860.
- Boehler, R., 1996. Melting temperature of the Earth's mantle and core: Earth's thermal structure, *Annu. Rev. Earth Planet. Sci.*, **24**(1), 15–40.
- Bogiatzis, P., Ishii, M. & Davis, T.A., 2016. Towards using direct methods in seismic tomography: computation of the full resolution matrix using high-performance computing and sparse QR factorization, *Geophys. J. Int.*, **205**(2), 830–836.
- Boschi, L., 2003. Measures of resolution in global body wave tomography, *Geophys. Res. Lett.*, **30**(19), doi:10.29/2003gl018222.
- Bozdağ, E., Peter, D., Lefebvre, M., Komatitsch, D., Tromp, J., Hill, J., Podhorszki, N. & Pugmire, D., 2016. Global adjoint tomography: first-generation model, *Geophys. J. Int.*, **207**(3), 1739–1766.
- Brown, J.M. & Shankland, T.J., 1981. Thermodynamic parameters in the Earth as determined from seismic profiles, *Geophys. J. Int.*, **66**(3), 579–596.
- Buffett, B.A., 2002. Estimates of heat flow in the deep mantle based on the power requirements for the geodynamo, *Geophys. Res. Lett.*, **29**(12), 7–17–4.
- Bull, A.L., McNamara, A.K. & Ritsema, J., 2009. Synthetic tomography of plume clusters and thermochemical piles, *Earth planet. Sci. Lett.*, **278**(3–4), 152–162.
- Bull, A.L., McNamara, A.K., Becker, T.W. & Ritsema, J., 2010. Global scale models of the mantle flow field predicted by synthetic tomography models, *Phys. Earth planet. Inter.*, **182**(3–4), 129–138.
- Bunge, H.-P., 2005. Low plume excess temperature and high core heat flux inferred from non-adiabatic geotherms in internally heated mantle circulation models, *Phys. Earth planet. Inter.*, **153**(1–3), 3–10.
- Bunge, H.-P. & Baumgardner, J.R., 1995. Mantle convection modelling on parallel virtual machines, *Comput. Phys.*, **9**(2), 207–215.
- Bunge, H.-P. & Davies, J.H., 2001. Tomographic images of a mantle circulation model, *Geophys. Res. Lett.*, **28**(1), 77–80.
- Bunge, H.-P., Richards, M.A. & Baumgardner, J.R., 1997. A sensitivity study of three-dimensional spherical mantle convection at 10^8 Rayleigh number: effects of depth-dependent viscosity, heating mode, and an endothermic phase change, *J. Geophys. Res. Solid Earth*, **102**(B6), 11 991–12 007.
- Bunge, H.-P., Richards, M.A., Lithgow-Bertelloni, C., Baumgardner, J.R., Grand, S.P. & Romanowicz, B., 1998. Time scales and heterogeneous structure in geodynamic Earth models, *Science*, **280**(5360), 91–95.
- Bunge, H.-P., Richards, M.A. & Baumgardner, J.R., 2002. Mantle-circulation models with sequential data assimilation: inferring present-day mantle structure from plate-motion histories, *Phil. Trans. R. Soc. A*, **360**(1800), 2545–2567.
- Bunge, H.-P., Hagelberg, C.R. & Travis, B.J., 2003. Mantle circulation models with variational data assimilation: inferring past mantle flow and structure from plate motion histories and seismic tomography, *Geophys. J. Int.*, **152**(2), 280–301.
- Cammarano, F., Goes, S., Vacher, P. & Giardini, D., 2003. Inferring upper-mantle temperatures from seismic velocities, *Phys. Earth planet. Inter.*, **138**(3–4), 197–222.
- Cammarano, F., Goes, S., Deuss, A. & Giardini, D., 2005. Is a pyrolytic adiabatic mantle compatible with seismic data?, *Earth planet. Sci. Lett.*, **232**(3), 227–243.
- Cammarano, F., Romanowicz, B., Stixrude, L., Lithgow-Bertelloni, C. & Xu, W., 2009. Inferring the thermochemical structure of the upper mantle from seismic data, *Geophys. J. Int.*, **179**(2), 1169–1185.
- Cammarano, F., Tackley, P.J. & Boschi, L., 2011. Seismic, petrological and geodynamical constraints on thermal and compositional structure of the upper mantle: global thermochemical models, *Geophys. J. Int.*, **187**(3), 1301–1318.
- Chemia, Z., Dolejš, D. & Steinle-Neumann, G., 2015. Thermal effects of variable material properties and metamorphic reactions in a three-component subducting slab, *J. Geophys. Res. Solid Earth*, **120**(10), 6823–6845.
- Christensen, U.R., 1995. Effects of phase transitions on mantle convection, *Annu. Rev. Earth Planet. Sci.*, **23**(1), 65–87.
- Christensen, U.R., 2001. Geodynamic models of deep subduction, *Phys. Earth planet. Inter.*, **127**(1–4), 25–34.
- Christensen, U.R., 2018. Geodynamo models with a stable layer and heterogeneous heat flow at the top of the core, *Geophys. J. Int.*, **215**(2), 1338–1351.
- Christensen, U.R. & Hofmann, A.W., 1994. Segregation of subducted oceanic crust in the convecting mantle, *J. Geophys. Res. Solid Earth*, **99**(B10), 19 867–19 884.
- Christensen, U.R. & Yuen, D.A., 1984. The interaction of a subducting lithospheric slab with a chemical or phase boundary, *J. Geophys. Res. Solid Earth*, **89**(B6), 4389–4402.
- Christensen, U.R. & Yuen, D.A., 1985. Layered convection induced by phase transitions, *J. Geophys. Res. Solid Earth*, **90**(B12), 10 291–10 300.
- Chust, T.C., Steinle-Neumann, G., Dolejš, D., Schuberth, B. S.A. & Bunge, H.-P., 2017. MMA-EoS: a computational framework for mineralogical thermodynamics, *J. Geophys. Res. Solid Earth*, **122**(12), 9881–9920.
- Cobden, L., Goes, S., Cammarano, F. & Connolly, J.A.D., 2008. Thermochemical interpretation of one-dimensional seismic reference models for the upper mantle: evidence for bias due to heterogeneity, *Geophys. J. Int.*, **175**(2), 627–648.
- Cobden, L., Goes, S., Ravenna, M., Styles, E., Cammarano, F., Gallagher, K. & Connolly, J.A.D., 2009. Thermochemical interpretation of 1-D seismic data for the lower mantle: the significance of nonadiabatic thermal gradients and compositional heterogeneity, *J. Geophys. Res. Solid Earth*, **114**(B11), doi:10.1029/2008jb006262.
- Cobden, L., Thomas, C. & Trampert, J., 2015. Seismic detection of post-perovskite inside the Earth, in *The Earth's Heterogeneous Mantle*, pp. 391–440, eds Khan, A. & Deschamps, F., Springer International Publishing.
- Cobden, L., Trampert, J. & Fichtner, A., 2018. Insights on upper mantle melting, rheology, and anelastic behaviour from seismic shear wave tomography, *Geochem. Geophys. Geosyst.*, **19**(10), 3892–3916.
- Cobden, L., Zhuang, J., Lei, W., Wentzcovitch, R., Trampert, J. & Tromp, J., 2024. Full-waveform tomography reveals iron spin crossover in Earth's lower mantle, *Nat. Commun.*, **15**(1), doi:10.38/541467-024-46040-1.
- Colli, L., Bunge, H.-P. & Schuberth, B.S.A., 2015. On retrodictions of global mantle flow with assimilated surface velocities, *Geophys. Res. Lett.*, **42**(20), 8341–8348.
- Colli, L., Ghelichkhan, S., Bunge, H.-P. & Oeser, J., 2018. Retrodictions of mid Paleogene mantle flow and dynamic topography in the Atlantic region from compressible high resolution adjoint mantle convection models: sensitivity to deep mantle viscosity and tomographic input model, *Gondwana Res.*, **53**, 252–272.
- Colli, L., Bunge, H.-P. & Oeser, J., 2020. Impact of model inconsistencies on reconstructions of past mantle flow obtained using the adjoint method, *Geophys. J. Int.*, **221**(1), 617–639.
- Connolly, J.A.D., 2005. Computation of phase equilibria by linear programming: a tool for geodynamic modelling and its application to subduction zone decarbonation, *Earth planet. Sci. Lett.*, **236**(1–2), 524–541.
- Connolly, J.A.D. & Khan, A., 2016. Uncertainty of mantle geophysical properties computed from phase equilibrium models, *Geophys. Res. Lett.*, **43**(10), 5026–5034.
- Cui, C. et al., 2024. GLAD-M35: a joint P and S global tomographic model with uncertainty quantification, *Geophys. J. Int.*, **239**(1), 478–502.
- Dannberg, J., Gassmüller, R., Li, R., Lithgow-Bertelloni, C. & Stixrude, L., 2022. An entropy method for geodynamic modelling of phase transitions: capturing sharp and broad transitions in a multiphase assemblage, *Geophys. J. Int.*, **231**(3), 1833–1849.
- Davies, D.R., Goes, S., Davies, J.H., Schuberth, B.S.A., Bunge, H.-P. & Ritsema, J., 2012. Reconciling dynamic and seismic models of Earth's lower mantle: the dominant role of thermal heterogeneity, *Earth planet. Sci. Lett.*, **353**–354, 253–269.
- Davies, D.R., Goes, S. & Lau, H.C.P., 2015. Thermally dominated deep mantle LLSVPs: a review, in *The Earth's Heterogeneous Mantle*, pp. 441–477, eds Khan, A. & Deschamps, F., Springer International Publishing.

- Davies, J.H. & Bunge, H.-P., 2001. Seismically “fast” geodynamic mantle models, *Geophys. Res. Lett.*, **28**(1), 73–76.
- Deal, M.M., Nolet, G. & van der Hilst, R.D., 1999. Slab temperature and thickness from seismic tomography: 1. Method and application to Tonga, *J. Geophys. Res. Solid Earth*, **104**(B12), 28 789–28 802.
- Deschamps, F. & Cobden, L., 2022. Estimating core–mantle boundary temperature from seismic shear velocity and attenuation, *Front. Earth Sci.*, **10**, doi:10.3389/feart.2022.1031507.
- Deschamps, F. & Trampert, J., 2003. Mantle tomography and its relation to temperature and composition, *Phys. Earth planet. Inter.*, **140**(4), 277–291.
- Deschamps, F., Trampert, J. & Snieder, R., 2002. Anomalies of temperature and iron in the uppermost mantle inferred from gravity data and tomographic models, *Phys. Earth planet. Inter.*, **129**(3–4), 245–264.
- Deschamps, F., Konishi, K., Fuji, N. & Cobden, L., 2019. Radial thermochemical structure beneath Western and Northern Pacific from seismic waveform inversion, *Earth planet. Sci. Lett.*, **520**, 153–163.
- Deuss, A., 2009. Global observations of mantle discontinuities using SS and PP precursors, *Surv. Geophys.*, **30**(4–5), 301–326.
- Dziewonski, A.M., 2005. The robust aspects of global seismic tomography, *Plates, Plumes and Paradigms*, Vol. **388**, eds Foulger, G., Natland, J.H., Presnall, D.C. & Anderson, D.L., Geological Society of America.
- Dziewonski, A.M. & Anderson, D.L., 1981. Preliminary reference Earth model, *Phys. Earth planet. Inter.*, **25**(4), 297–356.
- Farber, D.L., Williams, Q. & Ryerson, F.J., 1994. Diffusion in Mg₂SiO₄ polymorphs and chemical heterogeneity in the mantle transition zone, *Nature*, **371**(6499), 693–695.
- Fichtner, A. & van Leeuwen, T., 2015. Resolution analysis by random probing, *J. Geophys. Res. Solid Earth*, **120**(8), 5549–5573.
- Fichtner, A., Trampert, J., Cupillard, P., Saygin, E., Taymaz, T., Capdeville, Y. & Villaseñor, A., 2013. Multiscale full waveform inversion, *Geophys. J. Int.*, **194**(1), 534–556.
- Fichtner, A. et al., 2024. Seismic Tomography 2024, *Bull. seism. Soc. Am.*, **114**(3), 1185–1213.
- Flanagan, M.P. & Shearer, P.M., 1998. Global mapping of topography on transition zone velocity discontinuities by stacking SS precursors, *J. Geophys. Res. Solid Earth*, **103**(B2), 2673–2692.
- Forste, A.M. & Mitrovica, J.X., 2001. Deep-mantle high-viscosity flow and thermochemical structure inferred from seismic and geodynamic data, *Nature*, **410**(6832), 1049–1056.
- Forste, A.M., Dziewonski, A.M. & O’Connell, R.J., 1995. Thermal and chemical heterogeneity in the mantle: a seismic and geodynamic study of continental roots, *Phys. Earth planet. Inter.*, **92**(1–2), 45–55.
- Freissler, R., Zanolli, C., Lambotte, S. & Schuberth, B.S.A., 2020. Tomographic filtering via the generalized inverse: a way to account for seismic data uncertainty, *Geophys. J. Int.*, **223**(1), 254–269.
- Freissler, R., Schuberth, B.S.A. & Zanolli, C., 2024. A concept for the global assessment of tomographic resolution and uncertainty, *Geophys. J. Int.*, **238**, 992–1012.
- French, S.W. & Romanowicz, B., 2014. Whole-mantle radially anisotropic shear velocity structure from spectral-element waveform tomography, *Geophys. J. Int.*, **199**(3), 1303–1327.
- Frost, D.J., 2008. The upper mantle and transition zone, *Elements*, **4**(3), 171–176.
- Fukao, Y., Obayashi, M., Inoue, H. & Nenbai, M., 1992. Subducting slabs stagnant in the mantle transition zone, *J. Geophys. Res. Solid Earth*, **97**(B4), 4809–4822.
- Fukao, Y., Obayashi, M. & Nakakuki, T., 2009. Stagnant slab: a review, *Annu. Rev. Earth Planet. Sci.*, **37**(1), 19–46.
- Fullea, J., Lebedev, S., Martinec, Z. & Celli, N.L., 2021. WINTERC-G: mapping the upper mantle thermochemical heterogeneity from coupled geophysical–petrological inversion of seismic waveforms, heat flow, surface elevation and gravity satellite data, *Geophys. J. Int.*, **226**(1), 146–191.
- Gassmöller, R., Dannberg, J., Bangerth, W., Heister, T. & Myhill, R., 2020. On formulations of compressible mantle convection, *Geophys. J. Int.*, **221**(2), 1264–1280.
- Gheliikhhan, S., Bunge, H.-P. & Oeser, J., 2021. Global mantle flow retrodictions for the early Cenozoic using an adjoint method: evolving dynamic topographies, deep mantle structures, flow trajectories and sublithospheric stresses, *Geophys. J. Int.*, **226**(2), 1432–1460.
- Glšović, P., Forte, A.M. & Moucha, R., 2012. Time-dependent convection models of mantle thermal structure constrained by seismic tomography and geodynamics: implications for mantle plume dynamics and CMB heat flux, *Geophys. J. Int.*, **190**(2), 785–815.
- Goes, S., Govers, R. & Vacher, P., 2000. Shallow mantle temperatures under Europe from P and S wave tomography, *J. Geophys. Res. Solid Earth*, **105**(B5), 11 153–11 169.
- Goes, S., Cammarano, F. & Hansen, U., 2004. Synthetic seismic signature of thermal mantle plumes, *Earth planet. Sci. Lett.*, **218**(3), 403–419.
- Goes, S., Armitage, J., Harmon, N., Smith, H. & Huismans, R., 2012. Low seismic velocities below mid-ocean ridges: attenuation versus melt retention, *J. Geophys. Res. Solid Earth*, **117**(B12), doi:10.1029/2012jb009637.
- Grand, S.P., 1994. Mantle shear structure beneath the Americas and surrounding oceans, *J. Geophys. Res. Solid Earth*, **99**(B6), 11 591–11 621.
- Grand, S.P., van der Hilst, R.D. & Widiyantoro, S., 1997. Global seismic tomography: a snapshot of convection in the Earth, *GSA Today*, **7**, 1–7.
- Gu, Y.J. & Dziewonski, A.M., 2002. Global variability of transition zone thickness, *J. Geophys. Res. Solid Earth*, **107**(B7), ESE2–1–ESE2–17.
- Hager, B.H., Clayton, R.W., Richards, M.A., Comer, R.P. & Dziewonski, A.M., 1985. Lower mantle heterogeneity, dynamic topography and the geoid, *Nature*, **313**(6003), 541–545.
- Hayek, J.N., Vilacis, B., Bunge, H.-P., Friedrich, A.M., Carena, S. & Vibe, Y., 2020. Continent-scale hiatus maps for the Atlantic realm and Australia since the upper Jurassic and links to mantle flow induced dynamic topography, *Proc. R. Soc. A*, **476**(2242), doi:10.1098/rspa.2020.0390.
- Hirose, K., 2002. Phase transitions in pyrolytic mantle around 670-km depth: implications for upwelling of plumes from the lower mantle, *J. Geophys. Res. Solid Earth*, **107**(B4), ECV3–1–ECV3–13.
- Hirose, K., 2006. Postperovskite phase transition and its geophysical implications, *Rev. Geophys.*, **44**(3), doi:10.2929/2005rg000186.
- Hofmann, A.W. & Hart, S.R., 1978. An assessment of local and regional isotopic equilibrium in the mantle, *Earth planet. Sci. Lett.*, **38**(1), 44–62.
- Hoggard, M., Austermann, J., Randel, C. & Stephenson, S., 2021. Observational estimates of dynamic topography through space and time, in *Mantle Convection and Surface Expressions*, pp. 371–411, eds Marquardt, H., Ballmer, M., Cottaar, S. & Konter, J., AGU Geophysical Monograph Series.
- Holland, T.J.B., Hudson, N.F.C., Powell, R. & Harte, B., 2013. New thermodynamic models and calculated phase equilibria in NCFMAS for basic and ultrabasic compositions through the transition zone into the uppermost lower mantle, *J. Petrol.*, **54**(9), 1901–1920.
- Horbach, A., Bunge, H.-P. & Oeser, J., 2014. The adjoint method in geodynamics: derivation from a general operator formulation and application to the initial condition problem in a high resolution mantle circulation model, *GEM - Int. J. Geomath.*, **5**(2), 163–194.
- Ishii, T., Kojitani, H. & Akaogi, M., 2018. Phase relations and mineral chemistry in pyrolytic mantle at 1600–2200 °C under pressures up to the uppermost lower mantle: phase transitions around the 660-km discontinuity and dynamics of upwelling hot plumes, *Phys. Earth planet. Inter.*, **274**, 127–137.
- Ismail-Zadeh, A., Schubert, G., Tsepelev, I. & Korotkii, A., 2004. Inverse problem of thermal convection: numerical approach and application to mantle plume restoration, *Phys. Earth planet. Inter.*, **145**(1–4), 99–114.
- Ito, E. & Takahashi, E., 1989. Postspinel transformations in the system Mg₂SiO₄–Fe₂SiO₄ and some geophysical implications, *J. Geophys. Res. Solid Earth*, **94**(B8), 10 637–10 646.
- Jackson, I., Fitz Gerald, J.D., Faul, U.H. & Tan, B.H., 2002. Grain-size-sensitive seismic wave attenuation in polycrystalline olivine, *J. Geophys. Res. Solid Earth*, **107**(B12), ECV5–1–ECV5–16.
- Jarvis, G.T. & McKenzie, D.P., 1980. Convection in a compressible fluid with infinite Prandtl number, *J. Fluid Mech.*, **96**(3), 515–583.
- Jenkins, J., Cottaar, S., White, R.S. & Deuss, A., 2016. Depressed mantle discontinuities beneath Iceland: evidence of a garnet controlled 660 km discontinuity?, *Earth planet. Sci. Lett.*, **433**, 159–168.
- Karato, S., 1993. Importance of anelasticity in the interpretation of seismic tomography, *Geophys. Res. Lett.*, **20**(15), 1623–1626.

- Karato, S. & Karki, B.B., 2001. Origin of lateral variation of seismic wave velocities and density in the deep mantle, *J. Geophys. Res. Solid Earth*, **106**(B10), 21 771–21 783.
- Katsura, T., 2022. A revised adiabatic temperature profile for the mantle, *J. Geophys. Res. Solid Earth*, **127**(2), doi:10.2929/2021jb023562.
- Kellogg, J.B., Jacobsen, S.B. & O'Connell, R.J., 2002. Modelling the distribution of isotopic ratios in geochemical reservoirs, *Earth planet. Sci. Lett.*, **204**(1–2), 183–202.
- Kennett, B.L.N., Engdahl, E.R. & Buland, R., 1995. Constraints on seismic velocities in the Earth from traveltimes, *Geophys. J. Int.*, **122**(1), 108–124.
- Khan, A., Connolly, J. A.D. & Taylor, S.R., 2008. Inversion of seismic and geodetic data for the major element chemistry and temperature of the Earth's mantle, *J. Geophys. Res. Solid Earth*, **113**(B9), doi:10.2929/2007jb005239.
- Khan, A., Boschi, L. & Connolly, J. A.D., 2011. Mapping the Earth's thermochemical and anisotropic structure using global surface wave data, *J. Geophys. Res.*, **116**(B1), doi:10.1029/2010jb007828.
- Koelemeijer, P., Ritsema, J., Deuss, A. & van Heijst, H.J., 2016. SP12RTS: a degree-12 model of shear- and compressional-wave velocity for Earth's mantle, *Geophys. J. Int.*, **204**(2), 1024–1039.
- Koelemeijer, P., Schuberth, B.S.A., Davies, D.R., Deuss, A. & Ritsema, J., 2018. Constraints on the presence of post-perovskite in Earth's lowermost mantle from tomographic-geodynamic model comparisons, *Earth planet. Sci. Lett.*, **494**, 226–238.
- Kuskov, O., Kronrod, V. & Annerstein, H., 2006. Inferring upper-mantle temperatures from seismic and geochemical constraints: implications for Kaapvaal craton, *Earth planet. Sci. Lett.*, **244**(1–2), 133–154.
- Lawrence, J.F. & Shearer, P.M., 2006. A global study of transition zone thickness using receiver functions, *J. Geophys. Res. Solid Earth*, **111**(B6), doi:10.2929/2005jb003973.
- Lay, T., 2015. Deep earth structure: lower mantle and d", in *Treatise on Geophysics*, pp. 683–723, ed., Schubert, G., Elsevier.
- Lebedev, S., Schaeffer, A.J., Fullea, J. & Pease, V., 2017. Seismic tomography of the Arctic region: inferences for the thermal structure and evolution of the lithosphere, in *Circum-Arctic Lithosphere Evolution*, Vol. **460**, pp. 419–440, eds, Pease, V. & Coakley, B., Geological Society of London.
- Lebedev, S., Fullea, J., Xu, Y. & Bonadio, R., 2024. Seismic thermography, *Bull. seism. Soc. Am.*, **114**, 1227–1242.
- Leng, W. & Zhong, S., 2008. Controls on plume heat flux and plume excess temperature, *J. Geophys. Res. Solid Earth*, **113**(B4), doi:10.2929/2007jb005155.
- Lin, Y.-A., Colli, L. & Wu, J., 2022. NW Pacific-Panthalassa intra-oceanic subduction during mesozoic times from mantle convection and geoid models, *Geochem. Geophys. Geosyst.*, **23**(11), doi:10.2929/2022gc010514.
- Liu, Q. & Gu, Y.J., 2012. Seismic imaging: from classical to adjoint tomography, *Tectonophysics*, **566–567**, 31–66.
- Lobanov, S.S., Speziale, S. & Brune, S., 2021. Modelling Mie scattering in pyrolite in the laser-heated diamond anvil cell: implications for the core-mantle boundary temperature determination, *Phys. Earth planet. Inter.*, **318**, doi:10.1016/j.pepi.2021.106773.
- Long, M.D. & Becker, T.W., 2010. Mantle dynamics and seismic anisotropy, *Earth planet. Sci. Lett.*, **297**(3–4), 341–354.
- Masters, G., Laske, G., Bolton, H. & Dziewonski, A.M., 2000. The relative behaviour of shear velocity, bulk sound speed, and compressional velocity in the mantle: implications for chemical and thermal structure, in *Earth's Deep Interior: Mineral Physics and Tomography from the Atomic to the Global Scale*, Vol. **117**, pp. 63–87, eds, Karato, S.-I., Forte, A., Liebermann, R., Masters, G. & Stixrude, L., AGU Geophysical Monograph Series.
- Matas, J. & Bukowski, M.S.T., 2007. On the anelastic contribution to the temperature dependence of lower mantle seismic velocities, *Earth planet. Sci. Lett.*, **259**(1–2), 51–65.
- Mégnin, C., Bunge, H., Romanowicz, B. & Richards, M.A., 1997. Imaging 3-D spherical convection models: what can seismic tomography tell us about mantle dynamics?, *Geophys. Res. Lett.*, **24**(11), 1299–1302.
- Mittelstaedt, E. & Tackley, P.J., 2006. Plume heat flow is much lower than CMB heat flow, *Earth planet. Sci. Lett.*, **241**(1–2), 202–210.
- Müller, R.D. *et al.*, 2016. Ocean basin evolution and global-scale plate reorganization events since Pangea breakup, *Annu. Rev. Earth Planet. Sci.*, **44**(1), 107–138.
- Munch, F.D., Khan, A., Tauzin, B., van Driel, M. & Giardini, D., 2020. Seismological evidence for thermo-chemical heterogeneity in Earth's continental mantle, *Earth planet. Sci. Lett.*, **539**, doi:10.1016/j.epsl.2020.116240.
- Murakami, M., Hirose, K., Kawamura, K., Sata, N. & Ohishi, Y., 2004. Post-perovskite phase transition in MgSiO₃, *Science*, **304**(5672), 855–858.
- Murakami, M., Hirose, K., Sata, N. & Ohishi, Y., 2005. Post-perovskite phase transition and mineral chemistry in the pyrolitic lowermost mantle, *Geophys. Res. Lett.*, **32**(3), doi:10.1029/2004gl021956.
- Nerlich, R., Colli, L., Ghelichkhan, S., Schuberth, B.S.A. & Bunge, H.-P., 2016. Constraining central Neo-Tethys Ocean reconstructions with mantle convection models, *Geophys. Res. Lett.*, **43**(18), 9595–9603.
- Nolet, G., Grand, S.P. & Kennett, B.L.N., 1994. Seismic heterogeneity in the upper mantle, *J. Geophys. Res. Solid Earth*, **99**(B12), 23 753–23 766.
- Nolet, G., Montelli, R. & Virieux, J., 1999. Explicit, approximate expressions for the resolution and a posteriori covariance of massive tomographic systems, *Geophys. J. Int.*, **138**(1), 36–44.
- Nolet, G., Karato, S. & Montelli, R., 2006. Plume fluxes from seismic tomography, *Earth planet. Sci. Lett.*, **248**(3–4), 685–699.
- Papanagnou, I., Schuberth, B.S.A. & Thomas, C., 2022. Geodynamic predictions of seismic structure and discontinuity topography of the mantle transition zone, *Geophys. J. Int.*, **234**(1), 355–378.
- Piazzoni, A.S., Steinle-Neumann, G., Bunge, H. & Dolejš, D., 2007. A mineralogical model for density and elasticity of the Earth's mantle, *Geochem. Geophys. Geosyst.*, **8**(11), doi:10.1029/2007gc001697.
- Priestley, K. & McKenzie, D., 2006. The thermal structure of the lithosphere from shear wave velocities, *Earth planet. Sci. Lett.*, **244**(1–2), 285–301.
- Priestley, K. & McKenzie, D., 2013. The relationship between shear wave velocity, temperature, attenuation and viscosity in the shallow part of the mantle, *Earth planet. Sci. Lett.*, **381**, 78–91.
- Ramirez, F.D.C., Selway, K., Conrad, C.P. & Lithgow-Bertelloni, C., 2022. Constraining upper mantle viscosity using temperature and water content inferred from seismic and magnetotelluric data, *J. Geophys. Res. Solid Earth*, **127**(8), doi:10.2929/2021jb023824.
- Rawlinson, N., Pozgay, S. & Fishwick, S., 2010. Seismic tomography: a window into deep Earth, *Phys. Earth planet. Inter.*, **178**(3–4), 101–135.
- Rawlinson, N., Fichtner, A., Sambridge, M. & Young, M.K., 2014. Seismic tomography and the assessment of uncertainty, in *Advances in Geophysics*, pp. 1–76, ed., Dmowska, R., Elsevier.
- Richards, F.D., Hoggard, M.J., White, N. & Ghelichkhan, S., 2020. Quantifying the relationship between short-wavelength dynamic topography and thermomechanical structure of the upper mantle using calibrated parametrization of anelasticity, *J. Geophys. Res. Solid Earth*, **125**(9), doi:10.2929/2019jb019062.
- Richards, F.D., Hoggard, M.J., Ghelichkhan, S., Koelemeijer, P. & Lau, H.C., 2023. Geodynamic, geodetic, and seismic constraints favour deflated and dense-cored LLVPs, *Earth planet. Sci. Lett.*, **602**, doi:10.1016/j.epsl.2022.117964.
- Richards, M.A. & Hager, B.H., 1984. Geoid anomalies in a dynamic Earth, *J. Geophys. Res. Solid Earth*, **89**(B7), 5987–6002.
- Ringwood, A.E., 1968. Phase transformations in the mantle, *Earth planet. Sci. Lett.*, **5**, 401–412.
- Ritsema, J., van Heijst, H.J. & Woodhouse, J.H., 1999. Complex shear wave velocity structure imaged beneath Africa and Iceland, *Science*, **286**(5446), 1925–1928.
- Ritsema, J., van Heijst, H.J. & Woodhouse, J.H., 2004. Global transition zone tomography, *J. Geophys. Res. Solid Earth*, **109**(B2), doi:10.2929/2003jb002610.
- Ritsema, J., McNamara, A.K. & Bull, A.L., 2007. Tomographic filtering of geodynamic models: implications for model interpretation and large-scale mantle structure, *J. Geophys. Res. Solid Earth*, **112**(B1), doi:10.2929/2006jb004566.
- Ritsema, J., Xu, W., Stixrude, L. & Lithgow-Bertelloni, C., 2009. Estimates of the transition zone temperature in a mechanically mixed upper mantle, *Earth planet. Sci. Lett.*, **277**(1–2), 244–252.

- Ritsema, J., Deuss, A., van Heijst, H.J. & Woodhouse, J.H., 2011. S40RTS: a degree-40 shear-velocity model for the mantle from new Rayleigh wave dispersion, teleseismic traveltimes and normal-mode splitting function measurements, *Geophys. J. Int.*, **184**(3), 1223–1236.
- Romanowicz, B., 2003. Global mantle tomography: progress status in the past 10 years, *Annu. Rev. Earth Planet. Sci.*, **31**(1), 303–328.
- Romanowicz, B. & Durek, J.J., 2000. Seismological constraints on attenuation in the Earth: a review, in *Earth's Deep Interior: Mineral Physics and Tomography from the Atomic to the Global Scale*, Vol. **117**, pp. 161–179, eds Karato, S.-I., Forte, A., Liebermann, R., Masters, G. & Stixrude, L., AGU Geophysical Monograph Series.
- Schmerr, N. & Garnero, E.J., 2006. Investigation of upper mantle discontinuity structure beneath the central Pacific using SS precursors, *J. Geophys. Res. Solid Earth*, **111**(B8), doi:10.2929/2005jb004197.
- Schubert, G. & Tackley, P.J., 1995. Mantle dynamics: the strong control of the spinel-perovskite transition at a depth of 660 km, *J. Geodyn.*, **20**(4), 417–428.
- Schuberth, B.S.A. & Bigalke, T., 2021. From mantle convection to seismic observations: quantifying the uncertainties related to anelasticity, *Mantle Convection and Surface Expressions*, *Geophysical Monograph* 263, 1st edn, Chap. 4, pp. 97–119, Wiley.
- Schuberth, B.S.A., Bunge, H., Steinle-Neumann, G., Moder, C. & Oeser, J., 2009a. Thermal versus elastic heterogeneity in high-resolution mantle circulation models with pyrolite composition: high plume excess temperatures in the lowermost mantle, *Geochem. Geophys. Geosyst.*, **10**(1), doi:10.1029/2008gc002235.
- Schuberth, B.S.A., Bunge, H.-P. & Ritsema, J., 2009b. Tomographic filtering of high-resolution mantle circulation models: can seismic heterogeneity be explained by temperature alone?, *Geochem. Geophys. Geosyst.*, **10**(5), doi:10.2929/2009gc002401.
- Schuberth, B.S.A., Zanolli, C. & Nolet, G., 2012. Synthetic seismograms for a synthetic Earth: long-period P- and S-wave traveltime variations can be explained by temperature alone, *Geophys. J. Int.*, **188**(3), 1393–1412.
- Shearer, P.M., 2000. Upper mantle seismic discontinuities, in *Earth's Deep Interior: Mineral Physics and Tomography from the Atomic to the Global Scale*, Vol. **117**, pp. 115–132, AGU Geophysical Monograph Series.
- Shim, S.-H., 2008. The postperovskite transition, *Annu. Rev. Earth Planet. Sci.*, **36**(1), 569–599.
- Simmons, N.A., Forte, A.M. & Grand, S.P., 2006. Constraining mantle flow with seismic and geodynamic data: a joint approach, *Earth planet. Sci. Lett.*, **246**(1–2), 109–124.
- Simmons, N.A., Forte, A.M. & Grand, S.P., 2009. Joint seismic, geodynamic and mineral physical constraints on three-dimensional mantle heterogeneity: implications for the relative importance of thermal versus compositional heterogeneity, *Geophys. J. Int.*, **177**(3), 1284–1304.
- Simmons, N.A., Myers, S.C., Johannesson, G., Matzel, E. & Grand, S.P., 2015. Evidence for long-lived subduction of an ancient tectonic plate beneath the southern Indian Ocean, *Geophys. Res. Lett.*, **42**(21), 9270–9278.
- Simmons, N.A., Schuberth, B.S.A., Myers, S.C. & Knapp, D.R., 2019. Resolution and covariance of the LLNL-G3D-JPS global seismic tomography model: applications to traveltime uncertainty and tomographic filtering of geodynamic models, *Geophys. J. Int.*, **217**(3), 1543–1557.
- Simmons, N.A., Myers, S.C., Morency, C., Chiang, A. & Knapp, D.R., 2021. SPiRAL: a multiresolution global tomography model of seismic wave speeds and radial anisotropy variations in the crust and mantle, *Geophys. J. Int.*, **227**(2), 1366–1391.
- Sobolev, S.V., Zeyen, H., Stoll, G., Werling, F., Altherr, R. & Fuchs, K., 1996. Upper mantle temperatures from teleseismic tomography of French Massif Central including effects of composition, mineral reactions, anharmonicity, anelasticity and partial melt, *Earth planet. Sci. Lett.*, **139**(1–2), 147–163.
- Soldati, G. & Boschi, L., 2005. The resolution of whole Earth seismic tomographic models, *Geophys. J. Int.*, **161**(1), 143–153.
- Stacey, F.D., 1998. Thermoelasticity of a mineral composite and a reconsideration of lower mantle properties, *Phys. Earth planet. Inter.*, **106**(3–4), 219–236.
- Stixrude, L. & Lithgow-Bertelloni, C., 2007. Influence of phase transformations on lateral heterogeneity and dynamics in Earth's mantle, *Earth planet. Sci. Lett.*, **263**(1), 45–55.
- Stixrude, L. & Lithgow-Bertelloni, C., 2011. Thermodynamics of mantle minerals - II. Phase equilibria, *Geophys. J. Int.*, **184**(3), 1180–1213.
- Stixrude, L. & Lithgow-Bertelloni, C., 2021. Thermal expansivity, heat capacity and bulk modulus of the mantle, *Geophys. J. Int.*, **228**(2), 1119–1149.
- Stixrude, L. & Lithgow-Bertelloni, C., 2024. Thermodynamics of mantle minerals - III. The role of iron, *Geophys. J. Int.*, **237**(3), 1699–1733.
- Styles, E., Davies, D.R. & Goes, S., 2011. Mapping spherical seismic into physical structure: biases from 3-D phase-transition and thermal boundary-layer heterogeneity, *Geophys. J. Int.*, **184**(3), 1371–1378.
- Su, J., Houser, C., Hearn, J.W. & Deschamps, F., 2023. Tomographic filtering of shear and compressional wave models reveals uncorrelated variations in the lowermost mantle, *Geophys. J. Int.*, **234**(3), 2114–2127.
- Tackley, P.J., Stevenson, D.J., Glatzmaier, G.A. & Schubert, G., 1993. Effects of an endothermic phase transition at 670 km depth in a spherical model of convection in the Earth's mantle, *Nature*, **361**(6414), 699–704.
- Taiwo, A., Bunge, H.-P., Schuberth, B.S.A., Colli, L. & Vilacis, B., 2023. Robust global mantle flow trajectories and their validation via dynamic topography histories, *Geophys. J. Int.*, **234**(3), 2160–2179.
- Thomas, C. & Billen, M.I., 2009. Mantle transition zone structure along a profile in the SW Pacific: thermal and compositional variations, *Geophys. J. Int.*, **176**(1), 113–125.
- Thomas, C., Cobden, L. & Jonkers, A.R.T., 2022. D'' reflection polarities inform lowermost mantle mineralogy, *Geochem. Geophys. Geosyst.*, **23**(10), doi:10.2929/2021gc010325.
- Thrustarson, S., van Herwaarden, D.-P., Krischer, L., Boehm, C., van Driel, M., Afanasiev, M. & Fichtner, A., 2022. Data-adaptive global full-waveform inversion, *Geophys. J. Int.*, **230**(2), 1374–1393.
- Trampert, J., Vacher, P. & Vlaar, N., 2001. Sensitivities of seismic velocities to temperature, pressure and composition in the lower mantle, *Phys. Earth planet. Inter.*, **124**(3–4), 255–267.
- van der Hilst, R.D., Widiyantoro, S. & Engdahl, E.R., 1997. Evidence for deep mantle circulation from global tomography, *Nature*, **386**(6625), 578–584.
- van Mierlo, W.L., Langenhorst, F., Frost, D.J. & Rubie, D.C., 2013. Stagnation of subducting slabs in the transition zone due to slow diffusion in majoritic garnet, *Nat. Geosci.*, **6**(5), 400–403.
- Vilacis, B., Hayek, J.N., Stotz, I.L., Bunge, H.-P., Friedrich, A.M., Carena, S. & Clark, S., 2022. Evidence for active upper mantle flow in the Atlantic and Indo-Australian realms since the Upper Jurassic from hiatus maps and spreading rate changes, *Proc. R. Soc. A*, **478**(2262), doi:10.1098/rspa.2021.0764.
- Virieux, J. & Operto, S., 2009. An overview of full-waveform inversion in exploration geophysics, *Geophysics*, **74**(6), WCC1–WCC26.
- Waszek, L., Tauzin, B., Schmerr, N., Ballmer, M.D. & Afonso, J.C., 2021. A poorly mixed mantle transition zone and its thermal state inferred from seismic waves, *Nat. Geosci.*, **14**(12), 949–955.
- Xu, W., Lithgow-Bertelloni, C., Stixrude, L. & Ritsema, J., 2008. The effect of bulk composition and temperature on mantle seismic structure, *Earth planet. Sci. Lett.*, **275**(1–2), 70–79.
- Zanolli, C., 2016. Global seismic tomography using Backus–Gilbert inversion, *Geophys. J. Int.*, **207**(2), 876–888.
- Zanolli, C., Koelmeijer, P. & Lambotte, S., 2017. Toward seeing the Earth's interior through unbiased tomographic lenses, *Geophys. Res. Lett.*, **44**(22), 11 399–11 408.
- Zhang, Z., Stixrude, L. & Brodholt, J., 2013. Elastic properties of MgSiO₃-perovskite under lower mantle conditions and the composition of the deep Earth, *Earth planet. Sci. Lett.*, **379**, 1–12.

APPENDIX A: GEODYNAMIC INPUT MODEL

We use the global mantle circulation model of Nerlich *et al.* (2016). It is computed with the parallel finite element code *TERRA* (Bunge

& Baumgardner 1995; Bunge *et al.* 1998), which solves the conservation equations for momentum, mass and energy at infinite Prandtl number (i.e. no inertial forces) in a 3-D spherical shell. The model is discretized in an icosahedral mesh and incorporates ~ 80 million degrees of freedom in 129 equidistant radial layers, with lateral grid spacing of ~ 25 km at the surface, reducing to ~ 15 km at the core-mantle boundary (CMB). This parametrization is sufficient to simulate global mantle flow at Earth-like convective vigour (thermal Rayleigh number $\sim 2 \times 10^8$). Isochemical convection is simulated, assuming a constant pyrolitic composition throughout the spatio-temporal model evolution. Effects of compressibility are included in form of the truncated anelastic liquid approximation (e.g. Jarvis & McKenzie 1980). The model combines internal (~ 24 TW) and bottom heating (~ 12 TW), with prescribed thermal boundary conditions of 300 K at the surface and 4200 K at the CMB. In particular the CMB temperature is not well known for Earth, but a high associated CMB heat flux is supported by many studies (e.g. Boehler 1996; Buffett 2002; Bunge 2005; Mittelstaedt & Tackley 2006; Glišović *et al.* 2012; Christensen 2018; Lobanov *et al.* 2021) and consistent with the assumption that seismic mantle heterogeneity is primarily controlled by variations in temperature (Schuberth *et al.* 2009a, b; Davies *et al.* 2012). Tectonic plate reconstructions of the last 230 Ma (Müller *et al.* 2016) are incorporated as surface velocity boundary condition through sequential data-assimilation (Bunge *et al.* 2002). The characteristic length scales and magnitudes of temperature variations in the model are therefore largely independent of the (unknown) initial condition (Colli *et al.* 2015). The resulting present-day state of the model serves as the starting point in our closed-loop, with presumed Earth-like thermal structure in both amplitude and wavelengths due to the dense grid spacing together with the simulated high vigour of convection.

APPENDIX B: ANELASTIC CORRECTION

Following Karato (1993), seismic velocities are corrected for the contribution of anelasticity based on the *seismic quality factor* Q_s ,

determined from a radial Q -profile and 3-D temperature deviations from a 1-D reference according to:

$$Q_s(T) = Q_{\text{ref}} \cdot \omega^\alpha \cdot \exp\left(\frac{\alpha E}{R} \cdot \left(\frac{1}{T} - \frac{1}{T_{\text{ref}}}\right)\right) \quad (\text{B1})$$

with frequency ω , gas constant R , activation energy E and the frequency-dependence of anelasticity expressed by α . Both α and E are highly uncertain in the mantle. For this study, we take fixed values of $\alpha = 0.26$ and $E = 424$ KJ mol $^{-1}$, based on experiments on grain size dependence of Q_s in olivine polycrystals (Jackson *et al.* 2002) and in line with the study of Stixrude & Lithgow-Bertelloni (2007). Q_{ref} is taken from PREM. In accordance with PREM, we generally assume a seismic period of 1s and omit the term ω^α from the calculation. Using $Q_s(T)$ determined from eq. (B1), we can correct the elastic seismic velocities v_{El} from the thermodynamic models to obtain v_Q , the seismic velocity relevant in the seismic frequency band that includes the effects of anelasticity, as:

$$v_Q = v_{\text{El}} \cdot \left(1 - \frac{1}{2} \cot\left(\frac{\pi\alpha}{2}\right) \cdot \frac{1}{Q_s(T)}\right). \quad (\text{B2})$$

APPENDIX C: BULK COMPOSITION

Table C1. Oxide proportions (in mol%) of the chemical bulk compositions used in this study, a six-oxide pyrolite (NCFMAS), BOC and DM. Based on Chust *et al.* (2017) and Papanagnou *et al.* (2022).

Component	NCFMAS (mol%)	BOC (mol%)	DM (mol%)
MgO	49.85	15.11	56.17
FeO	6.17	6.59	5.71
CaO	2.94	14.39	0.99
Al ₂ O ₃	2.22	10.39	0.59
Na ₂ O	0.11	1.76	0.00
SiO ₂	38.71	51.76	36.54

APPENDIX D: ORDER OF REPARAMETRIZATION AND MINERALOGICAL FORWARD CONVERSION

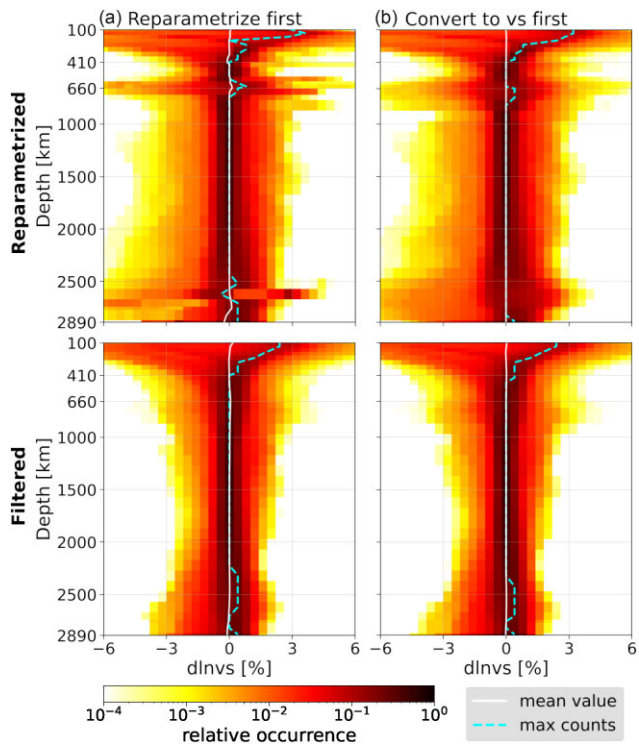


Figure D1. Depth-dependent histograms of seismic velocity perturbations after reparametrization and tomographic filtering for (a) initial reparametrization in the temperature-domain followed by mineralogical mapping to seismic velocities and (b) initial conversion to seismic velocities followed by reparametrization in the v_s -domain. Note that mapping from temperature to seismic velocities after reparametrization introduces strong heterogeneity around phase transitions in the velocity field, while reparametrizing after conversion considerably smoothes these effects. After tomographic filtering, very little of the initial differences remain, and the resulting histograms are almost identical. Tomographic filtering here is performed with the resolution operator of model S40RTS. The histograms are normalized as described in Fig. 2.

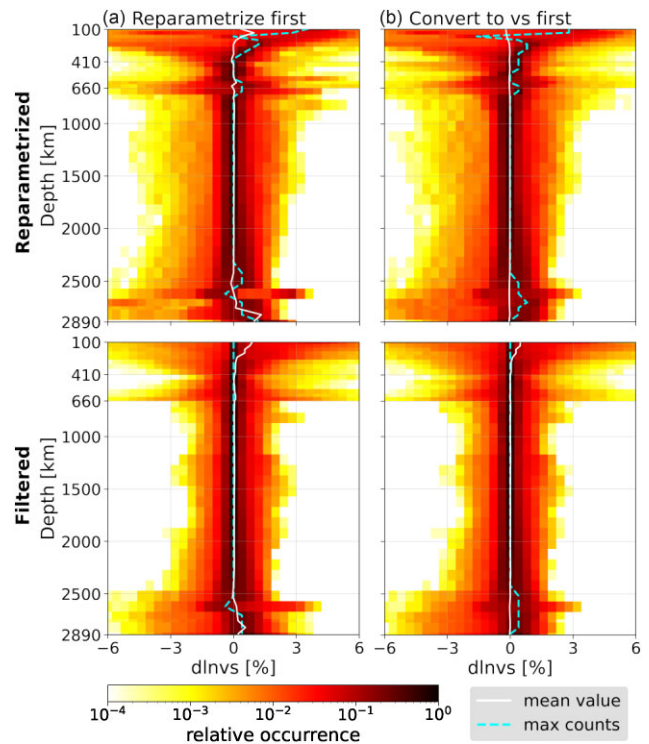


Figure D2. Same as Fig. D1, but with the tomographic filter for model LLNL.